Research Square

Preprints are preliminary reports that have not undergone peer review.
They should not be considered conclusive, used to inform clinical practice,
or referenced by the media as validated information.

Potential flow reconstruction of plunging breaking wave measured with PIV

Jeffrey Harris

jeffrey.harris@enpc.fr

Laboratoire d'Hydraulique Saint-Venant

Lili Kimmoun

Institut de Recherche sur les Phénomènes Hors Équilibre

Sunil Mohanlal

ADEC Engineering Consultancy

Jensen McTighe

University of Rhode Island

Jason Dahl

University of Rhode Island

Stephan Grilli

University of Rhode Island

Research Article

Keywords: breaking waves, potential flow, PIV

Posted Date: June 29th, 2026

DOI: https://doi.org/10.21203/rs.3.rs-10106145/v1

License: This work is licensed under a Creative Commons Attribution 4.0 International License.
Read Full License

Additional Declarations: No competing interests reported.

Potential flow reconstruction of plunging breaking wave measured with PIV

Jeffrey C. Harris[1*], Lili Kimmoun[2], Sunil Mohanlal[3], Jensen McTighe[4], Jason Dahl[4], Stephan Grilli[4]

[1*]LHSV, EDF R&D, ENPC, Institut Polytechnique de Paris, Chatou, France.
[2]IRPHE, Centrale Marseille, Marseille, France.
[3]ADEC Engineering Consultancy, Dubai, UAE.
[4]Department of Ocean Engineering, University of Rhode Island, Narragansett, 02882, RI, USA.

*Corresponding author(s). E-mail(s): jeffrey.harris@enpc.fr;
Contributing authors: sml@adecconsult.ae; jmctighe@uri.edu; jmdahl@uri.edu; grilli@uri.edu;

Abstract

Recent studies of steep and breaking waves have shown the importance of crest properties, and that there may be a quasi-universal breaking onset criterion based on the ratio $\boldsymbol{B = u_c/c_c}$. In the context of nonlinear potential flow models, such a precursor to breaking may be important for long-term simulations, which requires specifying energy dissipation, but in simulations, results are very sensitive to model parameters. In order to better understand this process, we study this question both numerically and experimentally. For a potential flow reconstruction, a fully nonlinear potential flow (FNPF) model that accurately reproduces the free-surface motion, even beyond wave overturning, is applied. Conditions reproduce experimentally generated plunging waves, with the water surface measured with wave gauges and a video camera, allowing for a particle image velocimetry (PIV) analysis. This PIV system provides fluid velocities close to the wave crest, at breaking onset, compare well with model results. It is observed that this $\boldsymbol{B = 0.85}$ criterion may be satisfied only when a wave has already started overturning.

Keywords: breaking waves, potential flow, PIV

1 Introduction

An improved understanding of breaking water waves — particularly of breaking onset and energy dissipation — is important for many applications [1, 2] and particularly for offshore structures whose design is often governed by the largest wave slamming loads that can occur [3]. While Computational Fluid Dynamics (CFD) models can accurately simulate breaking waves [4, 5] and their interaction with the seafloor or structures, these are extremely computationally demanding models whose use is usually restricted to small spatial and temporal scales. As a result, less costly reduced-order models, featuring simplifying the physics, have long been and are still widely used in ocean and coastal engineering design. These models, which simulate the processes affecting wave propagation with various degrees of fidelity (among many others) are those based on Saint-Venant [6], multi-layer Navier-Stokes [7, 8], Boussinesq [9], Serre-Green-Nagdhi [10], or fully nonlinear potential flow (FNPF) [11, 12] equations. In these models, energy dissipation related to breaking waves continues to be only approximately modeled, for instance, based on hydraulic jump analogies [13], eddy viscosity models [14], or more complex turbulence models, while breaking onset still needs to be identified based on simple wave parameters. This aspect, which has seen a lot of interest in recent years, is the focus of this paper.

In some ways it is worth noting that parameterizing breaking events with simple criteria is similar to earlier attempts, based on the mathematical approach of John [15], where many authors, such as New [16], Greenhow [17], Longuet-Higgins [18] derived analytic approximations to parts of the near-crest flows at certain stages of wave overturning. Such models can be related to geometric properties observed in the past by cine camera [19], but in more recent years, such parameterizations have not led to specific understanding of breaking criteria.

Many geometric, kinematic, or dynamic breaking onset criteria have been proposed. Derakhti et al. [5, 20] compared and reviewed those (to date) and showed that the recently proposed kinematic criterion, $B = u_c/c_c = B_t \simeq 0.85$, of Barthelemy et al. [21], appeared to be the most universal and discriminant of breaking onset for a wide range of water depth and wave characteristics (with u_c and $c_c = d\mathbf{x}_c/dt$ the water velocity and the crest and the crest celerity, respectively, with $\mathbf{x}_c(t)$ the crest location). This suggests that a wave in which the crest fluid velocity exceeds 0.85 times the crest phase velocity, will evolve to breaking and eventually overturn. A variety of works have attempted to assess both the accuracy and the universality of this criterion, including steepness or depth-limited breaking conditions, spilling or plunging conditions, and 2D or 3D wave conditions. To date, only a few exceptions were identified, such as by Scolan and Etienne [22] or Hasan et al. [23]. Notably, the example from Scolan and Etienne shows that both the $B = u_c/c_c$ and the vertical pressure gradient criterion, which is often used, cannot be considered completely universal. However, such studies show that, while mathematically the B-criterion may still be imperfect, it may be sufficient for most practical and realistic situations. In this paper, we attempt to assess this breaking onset criterion by comparing results of an accurate model to precision experiments.

Importantly, besides predicting breaking onset, other work, such as by Derakhti et al. [2], showed that the time-derivative of B at breaking onset, dB/dt for $B = B_t$

— i.e., how fast a wave crosses the threshold — when multiplied by an appropriate time-scale T_b, yields a breaking strength parameter γ, which correlates with the non-dimensional rate of energy dissipation b_γ, during the breaking event, thus,

$$\gamma = T_b \left.\frac{dB}{dt}\right|_{B=B_t} \qquad \text{and} \quad b_\gamma = 0.034\,(\gamma - 0.30)^{2.5}. \tag{1}$$

Mohanlal et al. [24] studied this type of parameterization as one of their breaking dissipation models for simulating shallow water waves propagating over a sloping bottom or a bar, in Grilli et al.'s 2D-FNPF model [25, 26], up to and including breaking; they both detected breaking onset using B and specified the breaking dissipation by way of an absorbing surface pressure [13, 27], and which seemed to indicate that Eq. (1) does not always provide the correct dissipation rate, especially in shallow water (more details will be provided later). Mohanlal et al.'s results showed that, in such conditions, the breaking intensity γ: (i) can be related to the crest celerity, and (ii) for a range of tests, also seems to predict the breaking type (e.g., spilling, plunging). Other studies showed that this parameter was also a predictor of the slamming force on a structure [3]. It is thus of interest to further investigate the relevance of the B criterion and, in general, to improve our understanding of the crest kinematics at breaking onset. In the present study, this is done through a comparison of results of precision laboratory experiments with simulations in a FNPF model in which the breaking dissipation is parameterized in a way similar to Mohanlal et al. [24].

One issue with the use of the B-criterion is that even though it is typically reached before the overturning of the wave crest, it is sufficiently close to this event that high resolution of the free surface — potentially combined with smoothing — may be required to accurately capture both the exact crest position and the fluid velocity at the crest [24, 28]. In practice, whether for experimental or numerical results, if the wave phase speed at the crest is computed by tracking the wave crest location $\mathbf{x}_c(t)$, one may still need filtering in order to produce consistent results [24, 29] — i.e., precisely locating the point of maximum wave elevation — but it can be difficult to verify whether this filtering affects the results obtained.

Wave propagation models based on FNPF theory — especially using a higher-order Boundary Element Method (BEM) in an Eulerian-Lagrangian framework — have been widely shown to be very accurate to simulate wave geometry and kinematics up to breaking [30–32]. In particular, such models were shown to accurately simulate overturning free surfaces, in both 2D and 3D [25, 26, 33, 34]. In fact, Barthelemy et al. [21] used results of simulations performed with Grilli et al.'s [35] 3D-BEM-FNPF model to propose the B criterion. Despite these advances in numerical modeling, there is little experimental evidence of the accuracy of these approaches to predict flow velocity near the crest at breaking onset, such as studied by Varing et al. [20] using a 2D-BEM-FNPF model. Clearly once wave overturning and breaking occur, viscous forces (and vorticity) become large and potential flow theory is no longer applicable. Before that stage, there may also be other concerns related to surface tension, varying air pressure, or other physics not usually represented in FNPF or other wave models with reduced-physics. Similar model-experiment comparisons have

been made previously to assess the performance of Boussinesq models for shoaling waves [36], or point measurements of velocity for focused waves [37].

One widespread method to measure flow velocity in experiments is the particle image velocimetry (PIV). However, while various theoretical and numerical estimates of the breaking crest kinematics have been made, including those involving the B-criterion, very few PIV measurements have been made in the high-crest region of waves, allowing to calculate quantities such as B over time and assessing their relevance for predicting breaking onset [38]. When Longuet-Higgins and Cokelet [39] performed the first simulation of overturning waves in a 2D-BEM-FNPF model, PIV measurements were not yet available. It took nearly two decades before the kinematics of shoaling waves was measured by Laser Doppler velocimetry (LDV) [40]; then Chang et al. [41] made one of the first PIV measurement of breaking wave kinematics, and Skyner [42] compared similar measurements in deep water plunging breakers to 2D-BEM-FNPF simulations — using Dold and Peregrine's [43] model, showing good agreement. Qiao and Duncan [44] performed a similar comparison for spilling breakers — for which there is also a crest overturning, but at small scale [31]; and other studies made similar comparisons for breaking waves in shallow water [45–49], or for 3D breaking waves [50]. PIV has also been used to study how wave momentum changes after breaking [51], and how turbulence is generated [52]. Based on this earlier work, it is generally recognized that accurately measuring the flow velocity at and near the crest of a breaking wave with the PIV is difficult, and results are affected by camera angle and image reflection [53–55].

Comparisons of PIV measurements with results of Navier-Stokes models have of course also be performed [56, 57], as well as very recently comparisons with openly available datasets [58], although one would expect from earlier work that FNPF model results should be sufficiently accurate for predicting wave properties at breaking onset and into the first stages of overturning, before the jet touches the free surface in front of the wave; this is unless one is also concerned with the flow of air above a breaking wave [59–61]. Additionally, using the FNPF approximation also avoids the added complexity of distinguishing numerical diffusion, which may be significant in Navier-Stokes solvers, from actual viscous effects.

In this work, with the aim to assess the relevance of the $B = u_c/c_c$ criterion, we perform a new set of experiments of overturning waves, in the precision wave flume of the Ecole Centrale de Marseille (ECM; now known as Centrale Méditerranée), and measure flow kinematics in the crest region using a PIV method. Furthermore, as there are to-date few measurements of γ, an important parameter to parameterize energy dissipation from breaking waves in reduced physics models [2, 24, 28], we also attempt to infer this parameter from experiments, which is difficult to do accurately [38, 62]. In doing so, we compare results obtained for different definitions proposed for the scaling parameter T_b. Indeed, Derakhti et al. [2] initially defined T_b based on the linear dispersion relationship and the distance between zero-crossings about the wave crest; as the latter might not be general this was later corrected [5], but alternative definitions were also proposed. Hulin et al. [28], for instance, based the value of T_b on the linear dispersion relationship and phase speed at the crest.

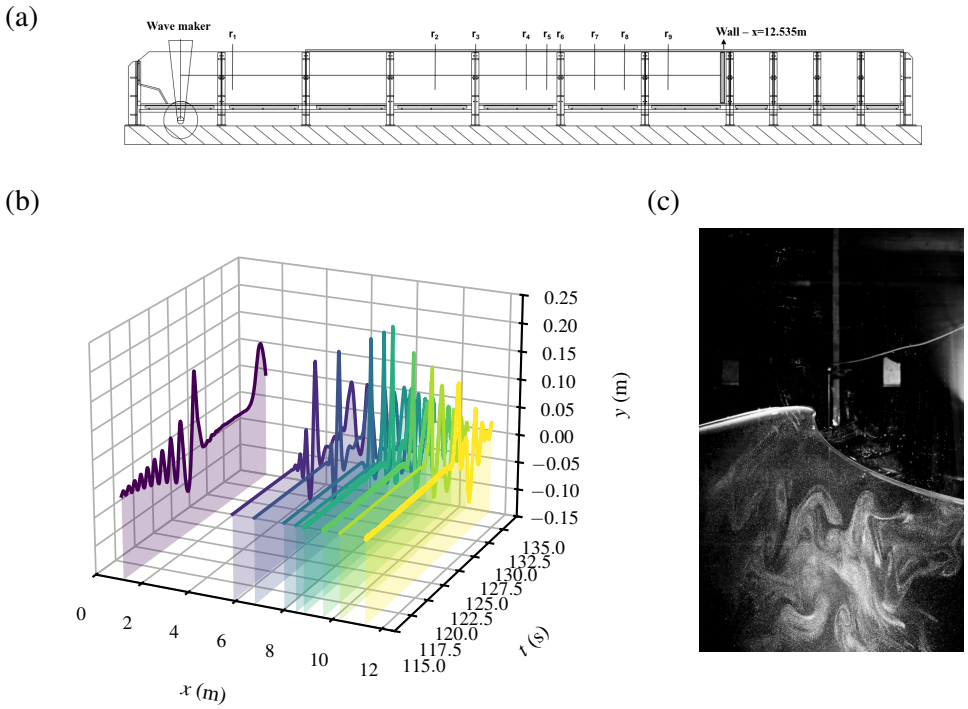


Fig. 1 (a) Vertical cross-section in the 12.535 m long (to the far-end wall) and 0.65 m wide section of the ECM precision wave flume used in experiments; positions r_1 to r_9 of nine wave gauges are marked with black arrows. (b) (right) Stacked diagram of typical time series of surface elevation of focused wave train measured at the nine wave gauges, with breaking occurring approximately 8 m from the wavemaker. (c) Typical focused breaking wave in experiments; the seeded PIV particles are visible in the water.

The PIV measurements, and derived parameters, will be compared with flow velocity and similar parameters simulated in a 2D-BEM-FNPF model [25, 26], based on which we will both identify and attempt to understand discrepancies between these approaches and their effect on the B-criterion. In this way, this work consolidates earlier efforts of using B and γ to improve breaking wave modeling in FNPF models, by [24] in the 2D-BEM of [25], and by [29], in the 3D-BEM of [12]. Note that similar, but more limited comparisons between this particular ECM wave flume and the 2D-BEM model has already been conducted for solitary waves [45].

In the following, the FNPF model is first briefly described, then the experimental setup and test program are presented, followed by an overview of the processing of the PIV data, to compute the fluid velocity field and the free-surface geometry. Finally, a comparison of the crest properties and internal fluid kinematics between PIV measurements and model results is given.

2 Laboratory experiments

Experiments were performed in a 12.535 m long (to the far-end wall) and 0.65 m wide section of the precision wave flume of École Centrale de Marseille (ECM), in which waves are generated using a flap-type wavemaker, with a paddle that rotates around an axis positioned 40 cm below the flume bottom (Fig. 1). A 50 cm diameter bumper located in the flume bottom-left corner prevents any impulsive motion of the paddle into the corner. For all experiments the water depth was $h = 0.667$ m, and wave elevation was measured using six resistance and three capacitance wave gauges at 300 Hz, at nine locations within the flume (Table 1). A high-speed video camera, located on the side of the flume approximately 8 m from the wavemaker recorded experiments at 200 Hz, i.e., both free surface geometry and tracer particle motions, for the PIV analysis as described below. A variety of large scale plunging breakers were created in the flume, using frequency focusing (see next subsection), until highly repeatable experiments were demonstrated, for which breaking onset occurred and the center of the camera viewing range.

2.1 Wavemaker motion for frequency focusing

Plunging breakers were generated in the laboratory flume in front of the video camera, by way of frequency focusing, in which shorter — slower — waves are first generated, followed by — faster — waves of gradually decreasing frequency. Amplitudes for these waves were extracted from a modified Ricker amplitude density spectrum — similar to a generalized Hermite-Gaussian function,

$$s(\omega) = A\sqrt{T}\, e^{-\omega^m T} \left[1 - \frac{\omega^m T - 1}{\omega_p^m T - 2}\right] \tag{2}$$

where $\omega_p = 2\pi/T_p$ is the peak angular frequency, m and T are spectral shape parameters, and A is a scaling factor. The Ricker spectrum is commonly used in geophysics and, for generating breaking waves, has also been used in simulations, for instance, by Lubin et al. [63] and Steer et al. [64].

Table 1 Wave gauge location and type in the ECM wave flume (represented by arrows in Fig. 1).

Wave gauge	x [m]	Type	Sensitivity [V/cm]
1	1.21	Resistance	0.5084
2	5.91	Resistance	0.4852
3	6.81	Resistance	0.5071
4	8.03	Resistance	0.5182
5	8.51	Resistance	0.4801
6	8.83	Capacitance	0.1783
7	9.62	Capacitance	0.1815
8	10.30	Resistance	0.4465
9	11.32	Capacitance	0.1639

Following Kimmoun et al. [65], the angular position of the wavemaker in a flume of depth h is calculated by linearly superposing $N = 4,096$ components of amplitude $a_n = s(\omega_n)\Delta\omega$ — obtained from the Ricker spectrum Eq. (2)) divided into N bins of angular frequency width $\Delta\omega$ — angular frequency ω_n, and wavenumber k_n, as,

$$\theta(t) = \sum_{n=1}^{N} \frac{a(\omega_n)}{C(\omega_n)} \sin\left(\omega_n(t - t_0) - k_n x_f\right) \qquad \text{with} \qquad \frac{\omega_n^2}{g} = k_n \tanh k_n h, \tag{3}$$

the linear dispersion relationship, where g is gravitational acceleration, and $C(\omega_n)$ denoting the linear transfer function for a flap wavemaker — as for instance derived by Sand and Mansard [66],

$$C(\omega_n) = \frac{2\sinh(k_n\, h)}{kh + \sinh(kh)\cosh(k_n\, h)} \left(\sinh(k_n\, h) + \frac{1 - \cosh(k_n\, h)}{k_n\,(h + l)}\right) \tag{4}$$

in which the "bumper" size $l = 0.5\,\text{m}$. In Eq. (3), the wave component phases $\varphi_n = k_n x_f$ are specified such that all the components (linearly) superimpose at a focal distance x_f at time t_f, as detailed below.

When performing frequency focusing experiments based on Eqs. (2-4), the scaling factor A is first determined numerically such that the theoretical maximum trough-to-crest height, at focusing, equals the target height H. Earlier work by Kimmoun et al. [65] showed that excellent repeatability of the generated wave trains, and breakers, could be achieved by limiting high-frequency motions of the wavemaker, which only caused spurious effects; this is further assessed in the next subsection. Additionally, to limit mechanical transients, the signal was windowed by a 14.14 s sine-taper at the start of motion, and a small constant phase offset centered the flap actuator displacement. At both the start and the end of each test, the paddle slowly reached its neutral position over a time $t_0 = 42.4264\,\text{s}$, which prevented the generation of spurious waves in the tank.

An example of the chirp-like angular displacements of the flap wavemaker paddle that results from this method is shown in Fig. 2. In this case, focusing occurs at $t_f = 127.2792\,\text{s}$, and no significant waves are present in the tank for $t \lesssim 107.3\,\text{s}$. When performing numerical experiments with the 2D-FNPF model, simulations will only be started beyond this time, when a measurable displacement of the paddle occurs.

2.2 Repeatability

In 2021, Dr. Kimmoun conducted sixteen focused wave breaking experiments in the ECM wave flume — with parameters listed in Table 2 — of which four tests (13, 14 15 and 19) will be discussed in detail hereafter and in Section 4, where they will be compared to numerical simulations in the NWT. [See Appendix A for images of similar experiments performed in the ECM wave flume in June 2018.] As shown in Table 2), all these tests were performed in nearly the same water depth $h = 0.667$ m and with the same peak spectral period $T_p = 2.4$ s and a target wave height only slightly changing in the range $H \in [0.2377, 0.2593]$ m. Using a Ricker spectrum and the linear superposition method described before, spectral parameters were iteratively

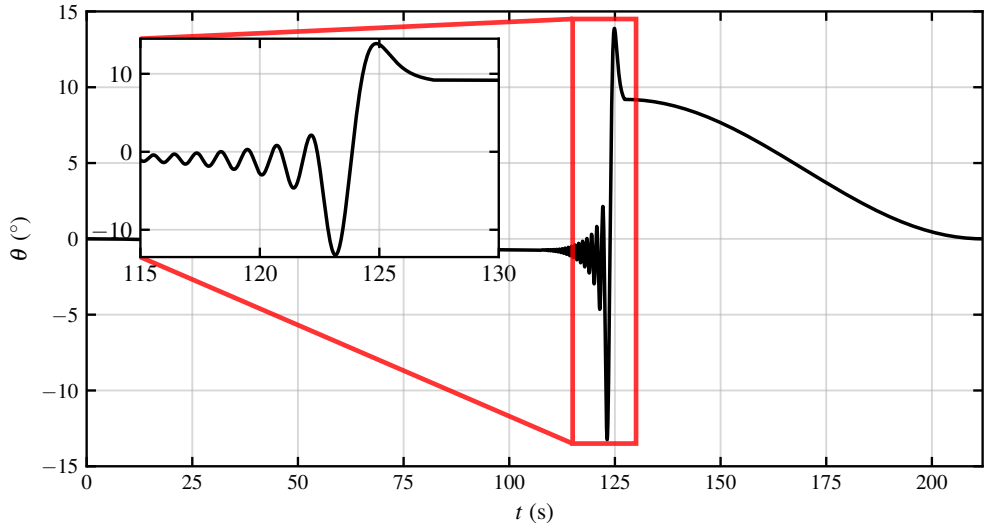


Fig. 2 Time series of angular displacement $\theta(t)$ of the wavemaker paddle specified for test 19. Note, to reduce computational time, the NWT simulations only start when the angular displacement becomes significant, which for this test is at $t = 107.3\,\mathrm{s}$.

Table 2 Parameters of focused breaking wave tests (conducted in 2021) in the ECM wave flume, with tests 13, 14, 15, and 19 (in gray) discussed in detail in the text. All tests were run for focused waves generated with the modified Ricker spectrum, for $T = 0.2285$, $m = 1.42$, and $T_p = 2.4\,\mathrm{s}$.

Test	h (m)	H (m)	x_f (m)	Δx (cm/px)	Free-surface level (px)
8	0.667	0.2377	8.0	0.03188	
9	0.667	0.2377	7.8	0.03188	920
10	0.667	0.2377	7.6	0.03188	920
11	0.667	0.2377	7.3	0.03188	920
12	0.667	0.2485	7.4	0.03188	920
13	0.667	0.2485	7.2	0.03188	920
14	0.667	0.2485	7.2	0.03188	1915
15	0.667	0.2485	7.2	0.03021	1915
16	0.667	0.2485	7.5	0.03021	1915
17	0.667	0.2593	7.5	0.03021	1915
18	0.667	0.2593	7.2	0.03021	1915
19	0.667	0.2593	7.8	0.03021	1915
20	0.666	0.2593	7.5	0.016445	2480
21	0.666	0.2593	7.2	0.016445	2480
22	0.667	0.2593	7.2	0.016445	2480
23	0.667	0.2593	7.8	0.016445	2480

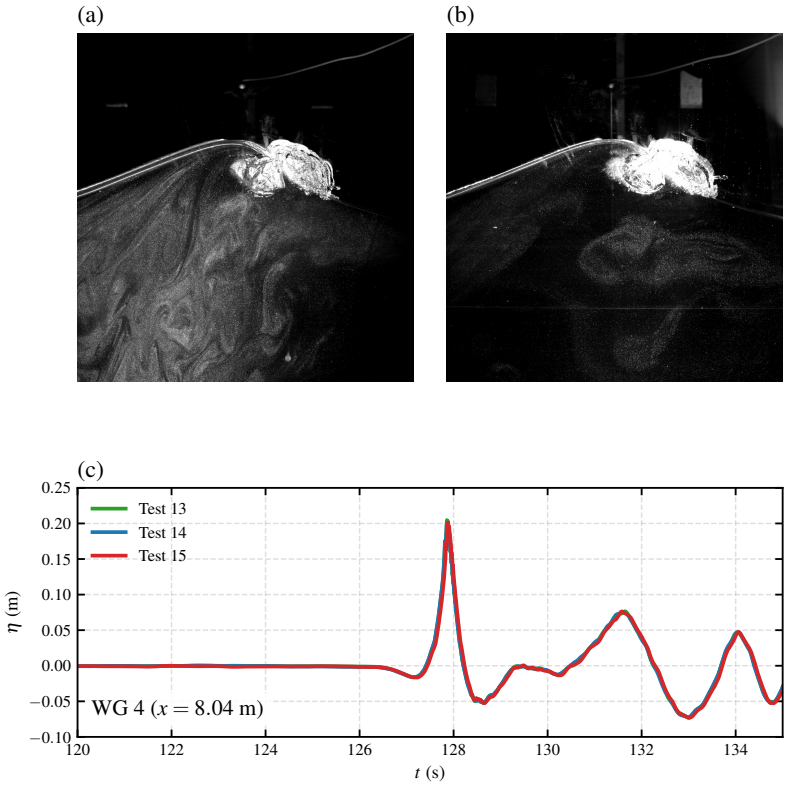


Fig. 3 Wave focusing tests experiments in the ECM wave flume, with identical input parameters (Table 2): (a,b) images of breakers in test 14 and 15, respectively, and (c) time-series of surface elevation measured at wave gauge 4 ($x = 8.03$ m), close to the focusing location, near the middle of each image in (a,b), for tests 13, 14, and 15, showing a high repeatability of these tests.

adjusted for the waves in each test to break at about the center of the camera viewing area, which yielded: $T = 0.2285$, $m = 1.42$, and a linear focusing distance varying in the range $x_f \in [7.2, 8.0]$ m; these adjustments were necessary because nonlinear waves propagate faster than linear waves and, hence, the actual focusing distance is different from x_f.

The repeatability of the tests was assessed by performing some of these twice and comparing their results. Figure 3, for example, compares results of tests 13, 14, and 15 (run on two different days), both visually and for the time series measured at wave gauge 4. These tests have identical parameters in Table 2, except for a shift in the PIV laser sheet position, causing a slight change in the pixel scaling parameter Δx. The images of each breaking wave in Fig. 3a,b appear to be highly similar, and the wave gauge measurements in Fig. 3c show very good repeatability; the maximum difference in the recorded wave elevation at the breaking point was only 0.5 mm, which is deemed to be sufficiently accurate for the purposes of this study. Note, this repeatability is even better than that reported in previous similar studies conducted in this tank [65].

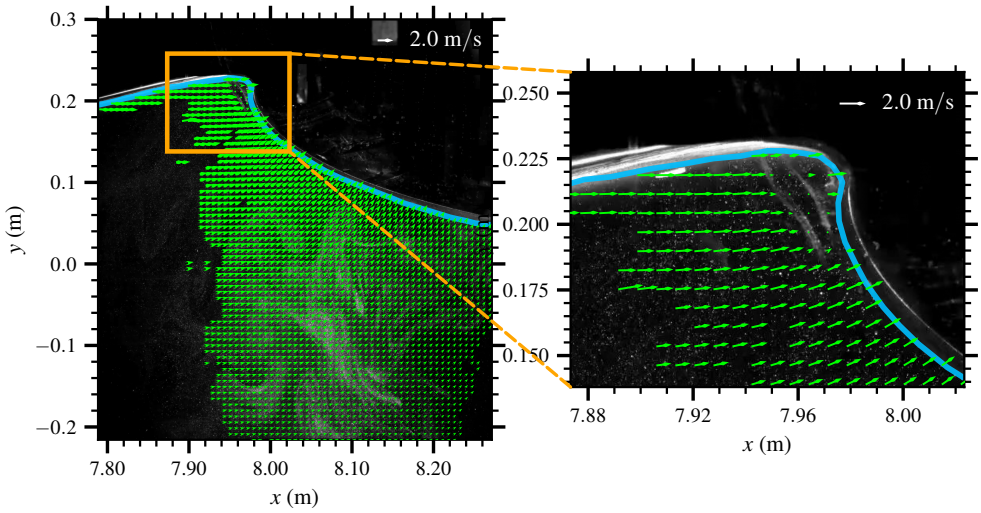


Fig. 4 (a) PIV image and (b) zoom around the crest, with reconstructed velocity field, for test 19, slightly beyond the breaking point, when the crest starts to overturn (just before it crosses wave gauge 4). Blue line indicates a manually-identified free-surface. Note, in a small area near the crest, velocities are either unavailable or appear to be noisy.

2.3 PIV processing

Particle Image Velocimetry (PIV) is used to measure velocity fields in fluids. The flow, seeded with small particles — acting as Lagrangian tracers of fluid motion — is illuminated by a thin laser sheet within a plane of interest. A high-speed video camera, installed on the side of the flume, captures two images of its field of view, at a small time interval Δt. By dividing the images into small interrogation windows and computing the spatial cross-correlation between corresponding regions in the two frames, the average particle displacement within each window is determined. Dividing these displacements by Δt yields the instantaneous velocity vectors in the measurement plane.

In this study, the processing of PIV data was made using the PIVMat v4.20 software; to aid with this processing, the free-surface was manually identified in the images and points outside of the water region were removed. Given the data available, in each test, 16 reconstructed velocity fields were retained for further analysis, starting at a time just before breaking onset of the wave. Figure 4 shows and example of the velocity field reconstructed for test 19, sightly beyond the breaking point, on top of the corresponding video image. Due to objects in the background (e.g., wave gauge 4), reflections, or scattering off the free surface, there is some noise in the reconstructed velocity vectors, particularly near and around the wave crest. However — and this will be the case in a number of other tests — the available data covers well the desirable area around the breaking crest.

Note, once overturning occurred, as for instance seen in Fig. 3, the free surface geometry is less accurately identifiable.

3 Numerical simulations

3.1 Model governing equations

The 2D-FNPF-BEM model of Grilli et al. [25, 26] — hereafter referred to as the Numerical Wave Tank (NWT) — was used to perform numerical simulations of selected experiments. While details of this model can be found in references, a summary of its governing equations is provided below.

Assuming an irrotational, inviscid, incompressible (potential) flow in the vertical plane (x, z), the fluid velocity is given by, $\mathbf{u} = \nabla\phi$, with ϕ the velocity potential. Mass conservation $\nabla \cdot \mathbf{u} = 0$ thus becomes Laplace's equation,

$$\nabla^2\phi = 0 \tag{5}$$

in the fluid domain Ω of boundary Γ, combining the free surface boundary $\Gamma_f(t)$, the bottom boundary Γ_b, the wave generation boundary $\Gamma_g(t)$, and the far-end boundary Γ_w.

On the free surface, the fully nonlinear kinematic and dynamic conditions are applied,

$$\frac{D\mathbf{r}}{Dt} = \frac{\partial\mathbf{r}}{\partial t} + (\mathbf{u}\cdot\nabla)\mathbf{r} = \mathbf{u} = \nabla\phi \qquad \text{on } \Gamma_f(t) \tag{6}$$

$$\frac{D\phi}{Dt} = -gz + \frac{1}{2}|\nabla\phi|^2 - \frac{p_a}{\rho} \qquad \text{on } \Gamma_f(t), \tag{7}$$

respectively — in a mixed Eulerian-Lagrangian formalism — where p_a is the atmospheric pressure, $\mathbf{r}$ denotes the position vector, and D/Dt is the material derivative.

Applying Green's second identity, Laplace's Eq. (5) is solved as the Boundary Integral Equation (BIE),

$$c(\mathbf{x}_k)\phi(\mathbf{x}_k) = \int_{\Gamma(\mathbf{x})} \left\{ \frac{\partial\phi}{\partial n}(\mathbf{x})\, G(\mathbf{x},\mathbf{x}_k) - \phi(\mathbf{x})\, \frac{\partial G}{\partial n}(\mathbf{x},\mathbf{x}_k) \right\} \mathrm{d}\Gamma, \tag{8}$$

in which $\mathbf{x}$ and $\mathbf{x}_k$ are points located on the boundary, $c(\mathbf{x}_k) = \alpha(\mathbf{x}_k)/(2\pi)$, with $\alpha(\mathbf{x}_k)$ the interior angle made by the boundary at point $\mathbf{x}_k$, $\mathbf{n}$ is the unit normal vector, pointing outward on the boundary, and,

$$G(\mathbf{x},\mathbf{x}_k) = -\frac{1}{2\pi}\ln r_k \quad \text{and} \quad \frac{\partial G}{\partial n}(\mathbf{x},\mathbf{x}_k) = -\frac{\mathbf{r}_k\cdot\mathbf{n}}{2\pi\, r_k^2} \tag{9}$$

are the 2D free space Green's function and its normal derivative, respectively, with $\mathbf{r}_k = \mathbf{x} - \mathbf{x}_k$ and $r_k = |\mathbf{r}_k|$.

Once the boundary fields, ϕ and $\partial\phi/\partial n$, are calculated by solving Eq. (8), the velocity field can explicitly be calculated, at any point $\mathbf{x}_i$ within the domain, as,

$$\mathbf{u}_i = \nabla_i \phi(\mathbf{x}_i) = \int_{\Gamma(\mathbf{x})} \left\{ \frac{\partial \phi}{\partial n}(\mathbf{x}) \{\nabla_i G(\mathbf{x}, \mathbf{x}_i)\} - \phi(\mathbf{x}) \{\nabla_i \frac{\partial G}{\partial n}(\mathbf{x}, \mathbf{x}_i)\} \right\} \mathrm{d}\Gamma, \tag{10}$$

in which $c(\mathbf{x}_i) = 1$, and the gradient of the Green's functions in Eq. (9) is calculated with respect to the interior point coordinates. In the present applications, in order to compare the numerical solution with the PIV measurements, velocity vectors are calculated over a Cartesian grid of internal points centered around the focal distance of the wave x_f.

Equations (8-9), together with relevant Dirichlet or Neumann boundary conditions (see next subsection), are solved using the Boundary Element Method (BEM), by discretizing the boundary Γ with K "collocation" nodes $\mathbf{x}_k$ and interpolating both the boundary geometry and the potential in between the nodes using higher-order boundary elements. On the free surface, nodes also represent water particles whose location and potential are time-updated by solving Eqs. (6) and (7) with a Lagrangian time stepping scheme [25, 26]. In Grilli et al.'s 2D-BEM model, this is done using second-order Taylor series expansions of both the node locations and their potential. Eqs. (6) and (7) provide the first-order terms in these expansions and their material derivative the second-order terms. In order to have the necessary fields to compute these terms, at each time step, a second Laplace's equation is solved for the time derivative of the potential, $\nabla^2(\partial\phi/\partial t) = 0$, using the same BIE (8) — since the domain geometry is identical — but boundary conditions for $\partial\phi/\partial t$ and $\partial^2\phi/\partial t \partial n$.

In Grilli et al.'s 2D-BEM model, various types of higher-order boundary elements can be used. Here, quadratic isoparametric elements are specified on the lateral and bottom boundaries of the domain, and cubic "Mid-interval-interpolation" (MII) elements are used on the free surface; the MII elements are defined over 4 nodes, but only their middle segment — or their first or last segment at boundary extremities — are used in integrations, ensuring local continuity of the boundary slope, which is important to accurately simulate overturning waves [26]. In simulations, to maintain a relatively constant density of points, the free surface is periodically regridded to an equal curvilinear spacing, as detailed in [26].

Integrals in Eqs. (8) and (10) are computed numerically within each element, using accurate Gaussian-like quadrature methods for both regular and singular integrals, and adaptive (subdivision) integration methods for quasi-singular integrals (occurring when two parts of the boundary are close to each other, e.g., in the tip of breaker jets) [26, 67]. Note, such quasi-singularity are even stronger (and hence require additional subdivisions) when computing the velocity field using Eq. (10), at interior points very close to the boundary, since the gradients of the Green's functions become hypersingular for points tending to the boundary. Finally, at the four corners of the domain, separating boundary segments with different boundary conditions (e.g., between the wavemaker and the free surface), extended compatibility conditions of the solution on both sides of the boundary are specified, which ensure continuity of both the potential and the velocity vector [26, 68]; combined with a double-node method, these conditions prevent numerical singularities from occurring.

3.2 Model boundary conditions

As the time-stepping scheme used in the model requires solving two Laplace's equation at each time step, in their BIE form (8), boundary conditions are required for both of these equations, which are detailed hereafter.

Typically, for wave propagation, the fluid domain has an impermeable bottom boundary Γ_b, on which a no-flow, Neumann boundary condition is specified. In the present applications, the far-end vertical boundary Γ_w, located at $x = 12.535\,\mathrm{m}$, is also impermeable, similar to the laboratory flume, hence, the same boundary conditions are used. Thus,

$$\mathbf{u}\cdot\mathbf{n} = \overline{\frac{\partial\phi}{\partial n}} = 0 \qquad \text{and} \qquad \overline{\frac{\partial^2\phi}{\partial t\,\partial n}} = 0 \quad \text{on } \Gamma_b, \Gamma_w \tag{11}$$

where the overlines indicate known values.

A flap wavemaker is used for generating waves on the leftward moving boundary $\Gamma_g(t)$. This is modeled using the boundary conditions by Grilli and Horrillo [69],

$$\overline{\frac{\partial\phi}{\partial n}} = r_g\frac{\partial\theta}{\partial t} \quad \text{on } \Gamma_g(t) \tag{12}$$

$$\overline{\frac{\partial^2\phi}{\partial t\,\partial n}} = r_g\frac{\partial^2\theta}{\partial t^2} + \frac{\partial\theta}{\partial t}\left(r_g\frac{\partial^2\phi}{\partial s^2} - \frac{\partial\phi}{\partial s}\right) \quad \text{on } \Gamma_g(t) \tag{13}$$

where (s, n) denote the tangential and normal directions, respectively, r_g is the distance between wavemaker nodes and the axis of rotation, and the second term in Eq. (13) results from the free slip — at velocity $u_s = \partial\phi/\partial s$ — along the wavemaker boundary. In the focused wave train applications, the time derivatives of the wavemaker angular displacement $\theta(t)$ are analytically calculated using Eq. (3). To shorten the simulation time, the slow initial motion of the paddle to its neutral position was ignored, therefore starting the simulation approximately 107.3 s along the time axis shown in Fig. 2.

Finally, the circular section seen in Fig. 1, which connects the flat bottom to the moving wavemaker paddle is also an impermeable boundary; in the model, it is considered as part of the bottom boundary Γ_b and, hence, included in the boundary conditions Eqs. (11). At each time step, the nodes along this curved boundary are regridded to an equal curvilinear spacing.

3.3 Breaking onset and energy dissipation

As discussed in the introduction, BEM-based FNPF models have been very successful and accurate in simulating overturning waves in 2D and 3D, whether caused by directional/frequency focusing or by a decreasing water depth [21, 25, 30, 31, 33, 37]; and this is shown in some of the simulations presented below. However, once the breaker jet impacts the free surface, potential flow theory no-longer applies and simulations have to be interrupted. This limitations was overcome by introducing an energy dissipation mechanism in FNPF models, through the application of an "absorbing" free

surface pressure in the dynamic free surface boundary condition Eq. (7). While there have been various formulations [13, 27, 69, 70], in Grilli et al.'s 2D-BEM-FNPF model, this pressure and the energy dissipated over a time step Δt take the form,

$$p_a(x,t) = \nu_a(t)\,\mathcal{S}(x)\frac{\partial \phi}{\partial n}(x,t) \quad \text{and} \quad E_D(t) = \Delta t \int_{x_l}^{x_r} p_a(x,t)\,\frac{\partial \phi}{\partial n}(x,t)\,\mathrm{d}x \tag{14}$$

respectively, where $\mathcal{S}(x)$ is a non-dimensional shape function (defined later), $\nu_a(t)$ is an absorption function, with the dimension of $\rho\, c$ (i.e., units of kg m^{-2} s^{-1}), and (x_l, x_r) is the boundary segment over which this pressure is specified — usually across part of the back and front of the breaking wave crest. Based on this definition of the absorbing pressure — proportional to the normal velocity of water particles at the free surface — the dissipated energy E_D is always positive. This type of absorbing pressure was used to design absorbing beaches in the model [69] or, in combination with a breaking onset criterion, to absorb energy of individual breaking waves [13, 27, 70]. In some of the earlier work done for spilling breakers[13, 27], breaking onset was detected based on a maximum wave front slope criterion, and energy dissipation was adjusted, through the $\nu_a(t)$ function, to match that in an inverted hydraulic jump [71].

More recently, as detailed in the introduction, Monhanlal et al. [24] implemented the B-breaking onset criterion — which was shown to be nearly universal — in Grilli et al.'s 2D-BEM-FNPF model. They simulated a variety of pre-existing experimental benchmarks — for periodic and irregular shoaling and breaking waves — using this criterion combined with the earlier dissipation based on the hydraulic jump analogy, but also using the newly formulated energy dissipation rate b_γ based on γ (see Eq. (1)), as well as a constant non-dimensional breaking strength b. Following the standard parameterization [44], we have,

$$\Pi_b(t) = \frac{b\,\rho}{g}\,c_c^5(t) \qquad \text{with} \quad E_D(t) = \Pi_b(t)\,\Delta t \tag{15}$$

Results showed, both of the latter formulations produced good results, but the simpler constant b value appeared to yield sufficiently accurate results across the fairly wide range of breaking intensities (or breaker types), for the benchmarks covered in shallow water.

Accordingly, in the present applications, to be able to compare model results with time series of surface elevation measured in the wave flume beyond the breaking point, the b-based dissipation method will be used in the 2D-BEM-FNPF model, with its value adjusted to obtain relevant numerical results (details will be given later). More specifically, there are three essential elements to the successful implementation of the breaker model: (i) accurately compute the breaking onset detection based on $B = u_c/c_c = B_t = 0.85$, hence the fluid velocity at the crest and the crest celerity, to identify where on the free surface (and when) a wave has reached a threshold beyond which breaking is inevitable; (ii) apply a physically relevant energy dissipation rate Π_b, to adequately damp waves identified as breaking; and (iii) apply a breaking termination criterion, to also identify when energy dissipation should end; in the work of Monhanlal et al. [24], this was $B_o = 0.4$ (o for "off"). Note that when a breaking

pressure is applied to the free-surface, this corresponds to a viscous component of the flow which does not appear in the surface velocity potential (and would formally appear in the rotational part of a Helmholtz decomposition), so B_o is a model-specific parameter, and does not necessarily correspond to a physical constraint. In the model, the absorbing pressure defined in Eq. (14) is applied around the impending breaking wave crest, once breaking onset is detected. As it takes time for this pressure to effectively damp the wave and prevent breaking, it is important to detect the instant of breaking onset and apply the absorbing pressure at that time, rather than wait to detect breaking itself to do so, as it would be too late to prevent wave overturning and the subsequent numerical instability in the model.

One challenging aspect of applying this dynamic breaking criterion is that it is local and first requires that all wave crests be identified and tracked at all times over the entire free surface Γ_f, and second that the crest celerity, $c_c = dx_c/dt$ be accurately computed . Accordingly, in the models, as in earlier work [13, 27, 72], the instantaneous celerity $c_c(t)$ of individual tracked wave crests is computed by fitting a moving polynomial to $x_c(t)$ over a time interval $[t - n\Delta t,\ t]$ (where n denotes the number of time steps involved in the curve fit), and taking the time derivative analytically in the polynomial. Details of the numerical method used to compute c_c can be found in [24].

For single valued free surface elevations $\eta(x,t)$, Eq. (14) yields,

$$\nu_a(t) = \frac{\Pi_b}{\int_{x_l}^{x_r} S(x)(\frac{\partial\phi}{\partial n})^2\sqrt{1+(\frac{\partial\eta}{\partial x})^2}\,\mathrm{d}x}. \tag{16}$$

in which the square root is the Jacobian, $d\Gamma/dx$. As in Grilli and Guignard's [27] work, the breaking crest segment (x_l, x_r) corresponds to locations near the wave troughs downstream and upstream of the considered wave, respectively, such that $|\frac{\partial\phi}{\partial n}| < \varepsilon\,|\frac{\partial\phi}{\partial n}|_{max}$, where $\varepsilon \ll 1$ (here $\varepsilon = 10^{-4}$). The shape function is smooth and such that $\mathcal{S}(x) \in [0,1]$ over the breaking region, with a ramp to ensure smooth transitions of p_a between zero in non-breaking regions and its calculated value in breaking regions [13, 27, 70], here,

$$\mathcal{S}(x) = \begin{cases} 0, & x \le x_l \\ \cos\left(\frac{\pi}{2}\frac{x-x_{l1}}{x_l-x_{l1}}\right), & x_l \le x \le x_{l1} \\ 1, & x_{l1} \le x \le x_{r1} \\ \cos\left(\frac{\pi}{2}\frac{x-x_{r1}}{x_r-x_{r1}}\right), & x_{r1} \le x \le x_r \\ 0, & x \ge x_r \end{cases} \tag{17}$$

where $x_{l1} = x_l + \alpha(x_r - x_l)$ and $x_{r1} = x_r - \alpha(x_r - x_l)$, $\alpha = 0.1$.

Breaking termination is also an important factor to accurately extract the appropriate amount of energy from breaking waves in the models. However, unlike in actual waves, as would for instance be simulated in a NS-VOF model [5], the value of B does not grow much beyond or remain above B_t in the FNPF model once dissipation is applied and a different method is required to detect breaking termination. To be

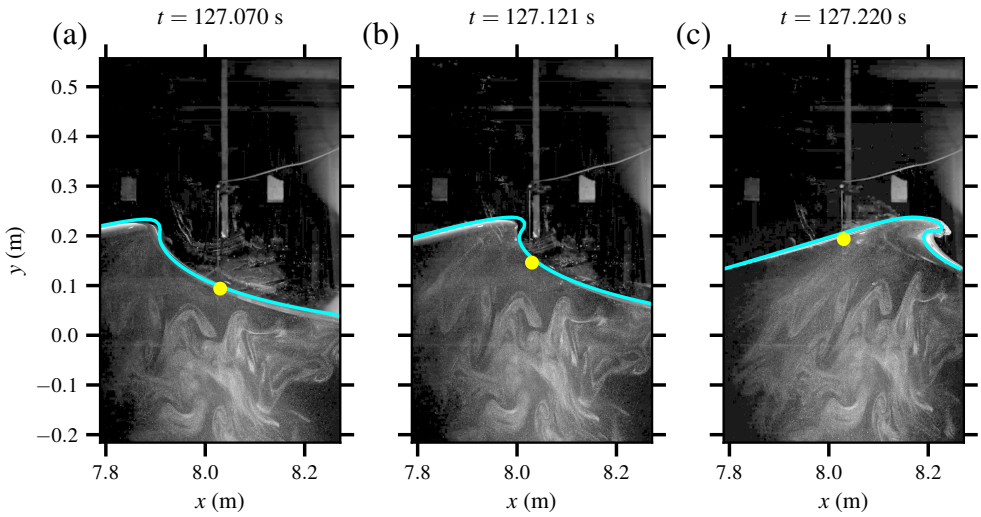


Fig. 5 Test 19 (Table 2). High-speed camera images of the experimental plunging breaker profile at three selected times $t = 127.070, 127.121$, and 127.220 s, from the breaking point onward. The blue line in each plot marks the corresponding free-surface computed in the NWT; for comparison, yellow bullets mark the surface elevation measured at each time at the wave gauge close to the frame center (WG 4).

consistent with the onset criterion, the termination criterion is based on B reaching a value B_o that is lower than the onset threshold, and needs to be calibrated based on benchmark data. For the applications considered here, the optimal B_o value appeared to be problem dependent. Specific values and their implications are discussed below.

4 Results and discussion

Experimental results were processed for each of the tests listed in Table 2 (i.e., camera frames and wave gauge time series) to extract the geometry of the free surface elevation as well as the internal velocity vectors (using the PIV algorithm). Fig. 5 for instance shows three frames extracted from the camera record of test 19 at three selected times $t = 127.070, 127.121$, and 127.220 s, while Fig. 6 shows time series of surface elevation measured at four wave gauges in the same test.

The NWT was run for the same initial wave conditions as listed in the table for each test, and numerical results were compared to experimental results. In this comparison, the effect on the breaking dissipation parameter on numerical results was first assessed by performing several simulations for test 19 with or without dissipation. Indeed, without dissipation, the NWT will simulate wave overturning, consistent with experiments, but simulations will be interrupted once the breaker jet impacts the free surface. As discussed earlier, the dissipation term is used in the NWT to be able to run the model beyond breaking and hence acquire longer time series of surface elevation, allowing for a longer comparison with experiments. In these runs, the NWT boundary was discretized with $N = 1584$ collocation nodes and $M = 1416$ elements, for an

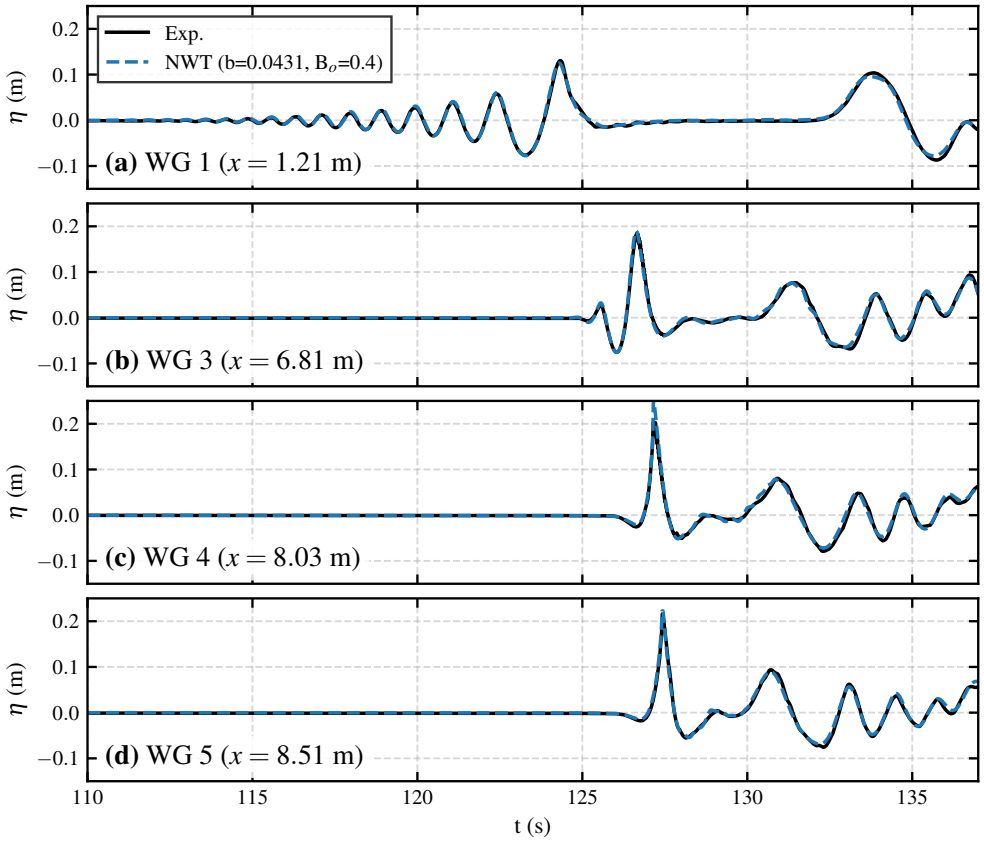


Fig. 6 Test 19 (Table 2). Comparison of time series of free surface elevation $\eta(t)$ at wave gauges (WG) 1, 3, 4 and 5 (Fig. 1a), measured in experiments (black, solid) and computed in the NWT (blue, dashed); WG 1 is closest to the wavemaker, while WG 3, 4 and 5 are located just before, at, and after the breaking point, respectively. Note that surface elevations shown at the right part of each plot includes waves reflected from the flume/NWT far side.

initial free-surface resolution of $\Delta x = 1\,\mathrm{cm}$; as indicated before, cubic MII elements were used on the free surface and quadratic isoparametric elements were specified on the other boundaries. The time-step was adaptively adjusted [26] as a function of the instantaneous minimum distance between nodes on the free surface $\Delta s_{\min}$, based on a constant Courant number $\mathcal{C}_0 \simeq 0.45$, as $\Delta t = \mathcal{C}_0\,\Delta s_{\min}/\sqrt{gh}$, where h is the flume depth and $\sqrt{gh}$ is the linear long wave celerity. Regridding of the free-surface at constant arclength Δs was done every 20 time-steps, yielding a slightly variable time-step $\Delta t \simeq 0.002\,\mathrm{s}$ in the NWT runs.

Regarding computational effort, as Grilli et al.'s NWT is not optimized nor implemented for parallel processing, each simulation was run on a single processor, yielding computational times of 18 hours for the test with breaking dissipation (to simulate up to $t \simeq 35\,\mathrm{s}$, until after breaking ends and the waves reflect from the far side of

the tank). The long computational time also results from considering the full non-linearity, both in the free surface boundary conditions and in the geometrical (i.e., moving wavemaker and free surface boundary), which requires recomputing at each time-step all the BEM interactions between nodes and elements. Other models could maybe simulate these tests much faster, but this FNPF-BEM NWT was developed to ensure high accuracy of the solution — hence preventing instabilities or the need for smoothing — and to model overturning waves without approximation; furthermore, by avoiding optimizations that depend on approximations such as the fast multipole method [12], this avoids compounding numerical errors more than necessary. When simulating solitary wave overturning on slopes with this model, Grilli et al. [26, 31] reported maximum errors on the wave volume and total energy on the order of 0.01%; similar or smaller errors were computed here at the end of each NWT simulation with the discretization detailed above.

As we will be comparing surface elevation snapshots and time series measured in experiments and computed in simulations, it is worth noting that no synchronization was made in doing so. The same wavemaker law of motion was specified in both the wave flume and the NWT and raw results acquired by the camera and the wave gauges were then compared to the NWT simulations. However, as indicated before, to reduce the computational time, the NWT simulations started at $t = 107.300\,\mathrm{s}$ after the wavemaker signal started being specified in the flume (at $t = 0$), when the paddle motion became significant (see Fig. 2). Furthermore, in analyzing experimental test results, it was determined that the wave gauges started recording 0.375 s before the wavemaker signal started (hence at absolute time $t = -0.375\,\mathrm{s}$) and the camera started recording at $t = 124.03\,\mathrm{s}$, only a few second before each wave breaking event occurred (to save on video storage). All experimental results were corrected to refer to absolute time t.

4.1 Free-surface comparison

Figure 5 compares free surface snapshots extracted from the camera record of test 19, measured with the camera to with the free surface shape computed at the same time — about the breaking time $t \simeq 127.1\,\mathrm{s}$ — in the NWT (without dissipation). These results appear to be in good agreement. For the same test, Fig. 6 compares the time series of surface elevation measured at wave gauges (WG) 1, 3, 4 and 5 to those computed in the NWT, with dissipation applied at breaking onset, when $B = B_c = 0.85$ (to be able to compute beyond breaking). First of all, in Fig. 5, comparing the WG 4 measurements made at the same times (yellow bullet) as the three free surface traces in the camera frames shows that these two types of measurements are fully consistent with each other as well as accurately synchronized. Then, comparing the complete experimental and numerical time series in Fig. 6 shows that these are in very good agreement prior to breaking onset, but also still in good agreement beyond breaking, confirming that the "artificial" dissipation applied in the NWT is able to approximate well the actual physical dissipation in the flume. The largest discrepancies between measurements and simulations occur near the breaking time t_b in WG 4, since the dissipation is applied prior to breaking and starts gradually reducing the wave elevation in a manner that does not fully match the actual breaking wave shape near the crest (e.g., Fig. 3).

Table 3 Focused breaking wave test 19. Wave parameters and kinematic states at breaking inset: (i) elevation η_b, (ii) characteristic period T_L based on linear wave theory (Eq. (24)), (iii) wavelength L_b (twice the distance between surface-crossing points around crest), (iv) characteristic period T_c based on crest celerity c_c, (v) (γ, b_γ) Derakhti et al.'s [2] breaking strength parameters (Eq. (1)), and (vi) b_S, Romero et al.'s [74] breaking strength parameter (Eq. (25)).

	Kinematic and dissipation properties						
$B = u_c/c_c$	η_b	T_L	L_b	T_c	γ	b_γ	b_s
0.85	0.235 m	1.85 s	4.12 m	1.70 s	3.64	0.693	0.0431

The exact peak at WG 4 also is not captured because the wave gauge attained the maximum value of 0.2029 m, so it was unable to capture the highest elevation. The calibration of the dissipation parameters is detailed in the next section, together with an analysis of crest properties.

The good agreement of the NWT simulations with measurements of the wave geometry — and phase — during overturning (Fig. 5) confirms, as concluded in earlier work [e.g., 30–32], that finely discretized FNPF simulations (here with $\Delta x \approx 1$ cm) can accurately simulate wave overturning until the instant the jet impacts the free surface. In fact, despite vast improvements in NS solvers in recent years, matching the breaking point can still be a challenging point for CFD models, requiring very high resolution in space and time [73].

Note that no specific parallax correction was applied to the video record, other than ensuring that the free-surface level — reported in pixels in Table 2 — was subtracted during the processing of frame frames. In the latter, an additional 70 pixel shift was applied to match the record with the illuminated plane in the middle of the tank.

4.2 Breaking crest properties

One of the goals of this study was to analyze the crest properties as the wave approaches breaking. Having confirmed that the NWT, without dissipation, can accurately model the overturning crest geometry (Fig. 5), the next step is to apply the breaking onset/dissipation method — previously validated in this NWT by Mohanlal et al. [24] — to allow computations to proceed beyond breaking. Identifying the instant when $B = u_c/c_c = B_t = 0.85$ in the model requires continuously computing the horizontal particle velocity at the crest, u_c, and the crest celerity $c_c = dx_c/dt$, where $x_c(t)$ denotes the crest position as a function of time; in the latter calculation, to avoid numerical noise, we apply the same smoothing algorithms as in Mohanlal et al.

Figure 7 shows, for test 19 (Table 2), the time series of crest kinematics properties computed with this method, with the addition of the maximum angle β of the wave front ahead of the crest; and Table 3 shows the crest parameters computed at breaking onset B_t. Looking closely at Fig. 7, we observe a difference between the time when $B = B_t = 0.85$ and the time when the wave front face becomes vertical, which occurs when $B \approx 0.83$, at only a slightly earlier time (0.02 s). This very small difference, in terms of the BEM solution, suggests that for standard wave models, such as based on vertical polynomials of the kinematics (e.g., HOS, Boussinesq, or otherwise), no

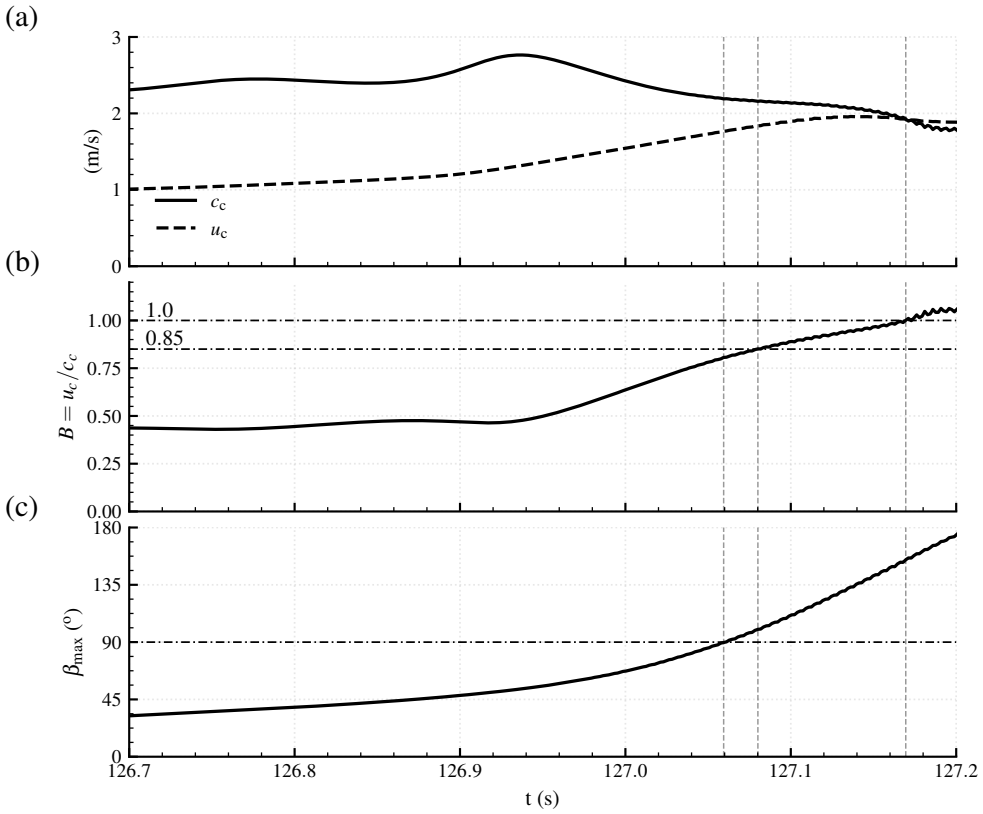


Fig. 7 Test 19 (Table 2). Time series of crest kinematics properties computed in the NWT: (top) horizontal particle velocity u_c (dashed line) and celerity c_c (solid line); (middle) Breaking onset criterion $B = u/c$ (solid line) compared to the threshold value $B_t = 0.85$ and the theoretical breaking point value $B_b = 1$ (dashed lines); and (bottom) maximum wave front angle $\beta_{\max}$ (solid line), with the dashed line marking $\beta_{\max} = 90°$ (when the wave front face is vertical).

matter the order of the vertical approximation, it would be impossible to resolve the instant the threshold B_t is reached prior to breaking, at least for this focused wave. Given that such an observation has not previously been reported, to the best of the authors' knowledge, it is likely limited to only rapidly breaking plunging breakers, but may be important in terms of some model developments.

Considering next the time evolution of the kinematic properties, notably, we see in Fig. 7 that this focused wave is strongly nonlinear for quite some time prior to the breaking event, with $B \in [0.4, 0.5]$. Further, as observed in many earlier studies [e.g., 5, 13, 75], following a monotonous increase prior to breaking ($B \leq B_b$), the crest particle velocity u_c shows a characteristic decrease beyond breaking. Similarly, the crest phase speed c_c, after continuously increasing up to a short time before breaking, shows a subsequent sharp decrease. Although some authors have searched for a specific explanation for these behaviors, no clear conclusion has emerged; however, based on

the definition of the crest used in the present work and in the context of potential flow theory, the following possible explanation can be proposed.

First, lets us define two Lagrangian time derivatives at the crest: (i) the standard material derivative,

$$\frac{D}{Dt} = \frac{\partial}{\partial t} + u\frac{\partial}{\partial x} + w\frac{\partial}{\partial z}, \tag{18}$$

which follows the water particle motion, and (ii) a crest-following time derivative,

$$\frac{d}{dt} = \frac{\partial}{\partial t} + c_c\frac{\partial}{\partial x} + w_c\frac{\partial}{\partial z}, \tag{19}$$

where c_c and w_c denote the horizontal and vertical crest celerity, respectively. Combining these two derivatives at the crest, applying the combined equation to u_c, and using the kinematic free surface boundary condition $w = w_c$, yields,

$$\frac{du_c}{dt} = \frac{Du_c}{Dt} + (c_c - u_c)\frac{\partial u_c}{\partial x} \tag{20}$$

(cf., Eq. (A.13) of [76]).

Now, for a constant atmospheric pressure, p_a, along the free-surface and given the dynamic free surface boundary condition $p = p_a$, the pressure gradient in the tangential direction $\mathbf{s}$ to the free surface vanishes: $\nabla p \cdot \mathbf{s} = 0$. Hence, for an inviscid fluid, the x-Euler equation at the crest ($\mathbf{s} = (1, 0)$) yields $Du_c/Dt = 0$, and,

$$\frac{du_c}{dt} = c_c\,(1 - B)\frac{\partial u_c}{\partial x}. \tag{21}$$

We note that, at the breaking point ($B = B_b = 1$), Eq. (21) yields $du_c/dt = 0$. Combining Eq. (21) with dB/dt from the definition of B at the crest further yields,

$$\frac{dB}{dt} = \frac{1}{c_c}\frac{du_c}{dt} - B\frac{1}{c_c}\frac{dc_c}{dt} = (1 - B)\frac{\partial u_c}{\partial x} - B\frac{1}{c}\frac{dc_c}{dt} \tag{22}$$

Evaluating this equation at breaking onset ($B = 1$), the horizontal strain term vanishes, leaving,

$$\left.\frac{dB}{dt}\right|_{B=1} = -\frac{1}{c_c}\frac{dc_c}{dt} \tag{23}$$

Based on this equation, since the phase speed is always positive ($c_c > 0$), for B to exceed 1, in post-breaking conditions, the crest must decelerate.

This is seen in Fig. 6, and was also observed in other works using the same definitions (cf. Fig. 3.20b in Hulin [77]). Due to the specific definitions of u_c and c_c, however, while not observed here, a wave could overturn without u_c/c_c ever exceeding unity. It is in part for these kinds of subtle points that we consider later the finer details of the kinematics at the crest.

4.3 Energy dissipation and breaking strength

In NWT simulations with energy dissipation, once breaking onset of a crest is detected (i.e., $B = B_t$), as described in Section 3.3, the absorbing pressure $p_a(x,t)$ is applied to the free surface section $x \in [x_l, x_r]$, defined around the crest, causing an energy dissipation $E_D(t)$ (see Eq. (14)). To accurately simulate both the energy dissipation and the corresponding reduction in crest elevation resulting from breaking, two parameters in the breaker model require tuning: (i) the B value corresponding to the breaking termination, B_o, when dissipation may be considered to be negligible and the flow to be approximately potential again, and (ii) the nondimensional breaking strength, b (see Eq. (15)). For the latter parameter, various studies have used either the instantaneous or average dissipation rate, as well as different values for the crest celerity. Here we use a constant b value but a time-varying $\Pi_b(t)$, based on a crest celerity corresponding to the instantaneous speed of motion of the crest location $x_c(t)$. As discussed by Mohanlal et al. [78], more tests were conducted than are presented here to optimize these two parameter values.

As discussed in the introduction, Derakhti et al. [2], in their NS simulations of focused breaking waves, noted that $dB(t)/dt$ at breaking onset was correlated with the breaking power dissipated in the model, averaged from breaking onset to termination, $\langle \epsilon \rangle$. On this basis, they developed a parameterization of the corresponding average breaking strength, $\langle b \rangle$, noted $b_\gamma(\gamma)$ (see Eq. (1)), in which γ was computed based on a breaking wave period,

$$T_b = \frac{L_b}{c_{lb}} \qquad \text{with} \qquad c_{lb} = \sqrt{g \frac{\tanh k_b h_b}{k_b}}, \tag{24}$$

the linear wave celerity at breaking in depth h_b, $k_b = 2\pi/L_b$, and L_b a relevant breaking wavelength calculated based on the method proposed by [5]. In this method, L_b is taken as twice the distance between the two zero-crossing points surrounding the breaking crest — except for particularly long waves, for which an equivalent zero-crossing distance is computed (cf., Fig. A2 in [5]).

In this work, the b_γ parameterization of dissipation was first used in NWT simulations, together with Eq. (24) and breaking onset identified based on the crest properties calculated using Mohanlal et al.'s [24] method, as detailed in Section 4.2. Using these various methods, in the simulations of test 19, for instance, yields $\gamma = 3.64$ and $b_\gamma = 0.693$ (Table 3). The latter, however, is quite a large breaking strength value, resulting from the intense and rapid focused wave breaking, which is outside of the range of values used by Derakhti et al. in their curve fit of NS model results yielding Eq. (1). As a result, applying this large b_γ value led to nonphysical results in the NWT. [Note, others [28] have since reported γ values nearly as large, suggesting that strongly plunging breakers can easily attain this value.]

To derive a more realistic $\langle b \rangle$ value for our focused wave test cases, we considered the breaking strength parameterization of Romero et al. [74] who, by studying a large set of experimental results, developed an empirical relationship for predicting the breaking strength as a function of the maximum linear wave steepness, $s = \sum_{n=1}^{N} a_n k_n$ of the incident wave train — where here (a_n, k_n) denote the focused wave component

amplitudes and wavenumbers, respectively from Eq. (3) — as,

$$b_s = 0.4(s - 0.08)^{5/2}, \tag{25}$$

which was derived in a way consistent with the inertial scaling and measurements of [79]. [Note, they also proposed a second formula, but for the range of s of the test cases seen here, the difference between the two is less than 5%.] Applying this formula to test 19, we find $s = 0.49$ from the wavemaker input data, and estimate the much smaller breaking strength value, $b_s = 0.0431$ (Table 3).

To assess the relevance of this b_s value, since we have both the NWT and experimental time-series of each wave gauge, we study the wave elevation measured at WG 5 ($x = 8.51\,\mathrm{m}$) and compare the root mean square error (RMSE) of the NWT and tank data in between two zero up-crossings located around the largest (breaking) wave (Fig. 8). By running the NWT for various combinations of b and B_o values, we find that the lowest RMSEs are obtained for a narrow range of these parameters' values (Table 4). This is to be expected since no time-variation of b is specified and the aim of the breaking model is thus simply to dissipate an amount of energy matching that of the physical breaking dissipation. Hence, a similar amount of energy can be dissipated in the NWT using a smaller dissipation rate over a longer time (i.e., a small b but also a small B_o) or a larger dissipation rate over a shorter time (i.e., a larger b but also a large B_o). Some unexpected results, however, can be seen in Table 4, such as using the largest dissipation rate $b = 0.3444$ with the smallest $B_\mathrm{o} = 0.3$ causes the NWT to become unstable, but not when using larger B_o values. This is not due to the main breaking event of interest here, but to instabilities occurring at other spurious points in the NWT. Nonetheless, Table 4 shows that the optimum combination of parameters yielding the smallest RMSE is $b = b_s = 0.0431$ (consistent with Eq. (25)) and $B_\mathrm{o} = 0.4$), which was retained. Looking at the time-series itself in Fig. 8, the optimum value from this sensitivity study does appear to provide the best visual agreement as well with the laboratory measurements.

The optimal combination of parameters identified in this sensitivity analysis is also consistent with results reported by Mohanlal [78], who followed the approach of Rapp and Melville [80] (which was also used later by Drazen et al. [79] and Tian et al. [81]). In that approach, the energy dissipation E_D is estimated by comparing the variance of the free-surface elevation, $\eta_{rms}^2 = \overline{\eta^2}$, measured upstream and downstream of the breaking event. Under linear wave theory, the time-averaged energy of a wave train is proportional to this variance ($\overline{E} = \rho g\, \eta_{rms}^2$). Although this relation is approximate for nonlinear waves, η_{rms}^2 can be readily computed from both experiments and NWT simulations at gauges located upstream and downstream of the breaking point, with their difference providing an estimate of dissipated energy. For test 19 here, the variability of this integral measure was very small in terms of different parameters, and so the RMSE was used to more clearly study the parameter sensitivity.

Having established a physically relevant breaking-dissipation model, the simulations can be propagated forward in time — including the post-breaking regime — and the model provides complete time series at the wave gauge locations, enabling further comparison with experiments. As shown in Fig. 6 for test 19, the agreement remains very good beyond the focusing time. In this later stage, the measured signal includes

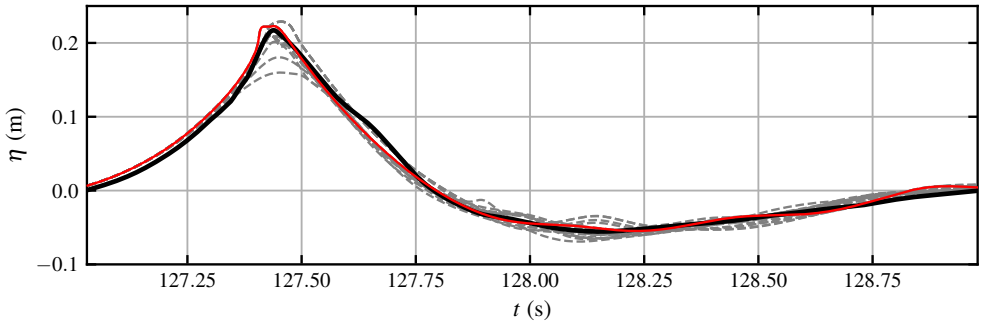


Fig. 8 Test 19. Free surface time series at WG 5 ($x = 8.51$ m) for varying damping parameters , such as listed Table 4: black solid line (experiment), gray dashed lines (NWT tests), and red solid line (optimum combination, $b_s = 0.0431$ and $B_o = 0.4$).

Table 4 Focused breaking wave test 19. Root mean square error (RMSE) of $\eta(t)$ (in cm) simulated in the NWT at WG5 ($x = 8.51$ m) compared to experimental measurement for various combinations of parameters b and B_o. Time averages are computed between the first two zero up-crossings at the experimental gauge, from 127.03 s to 128.93 s. Four simulations broke down (denoted by —), either due to insufficient damping or to spurious waves.

	Dissipation rate parameter (b)				
Offset (B_o)	**0.0215**	**0.0431**	**0.0861**	**0.1722**	**0.3444**
0.30	—	0.715	0.761	0.949	—
0.35	—	0.742	0.740	0.932	1.368
0.40	—	**0.715**	0.740	0.808	1.046
0.45	0.818	0.721	0.742	0.776	0.963

both incident (non-breaking or breaking) waves and, increasingly with time, broken waves that have reflected from the far wall. Additional wave gauge data for test 19, as well as the full dataset for other tests, are provided in the Supplementary Materials.

4.4 Computation of internal velocity field near the crest

Once the solution is calculated at time t in the NWT, the corresponding velocity field can be explicitly computed at arbitrary internal points $\mathbf{x}_i$ using the BEM Eq. (10) and compared to velocities measured with the PIV method in experiments. Making a quantitative comparison of these velocities requires that they be computed in the NWT at the same locations $\mathbf{x}_i$ as in experiments. However, as can be seen for instance in Fig. 4, the PIV data has gaps and, in particular, measurements are not sufficiently resolved or smooth near the crest to make this comparison possible at all the NWT internal points, if say they were defined on a regular grid. While advanced gap-filling algorithms could be applied, such as using the velocity divergence [82], hereafter we propose a reduced-order, but sufficiently accurate, analytic representation of the near-crest velocity. Moreover, applying Eq. (10) at points located very close to the free

Table 5 Complex pole locations (z_k) and strength (R_k) computed with Eq. (27) based on the flow kinematics simulated in the FNPF-BEM-NWT for test 19, at $t = 126.951\,\mathrm{s}$, when $B \simeq 0.5$. For the background flow, $U_b = -0.037\,\mathrm{m/s}$, $\dot{U}_b = -1.475\,\mathrm{m/s^2}$, and the Bernoulli coefficient is $C_0 = 23.83\,\mathrm{m^2/s}$.

	z_k (m)		$\dot{z}_k$ (m/s)		R_k ($\mathrm{m^2/s}$)		$\dot{R}_k$ ($\mathrm{m^2/s^2}$)	
Pole (k)	Re	Im	Re	Im	Re	Im	Re	Im
1	7.763	0.257	1.609	-0.219	-0.098	-0.018	0.399	0.299
2	7.859	0.725	3.996	-6.297	-0.393	0.036	7.399	-3.061
3	7.061	0.959	-1.165	-3.432	0.679	0.005	-9.393	0.096

surface creates quasi-singular integrals that require to be very accurately computed numerically, which is computationally demanding [67]. The analytic approach does not have this problem.

In simulations performed with an earlier implementation of this NWT, to avoid quasi-singular integrals and noting that for long waves velocities varied more smoothly in the vertical than in the horizontal direction, Grilli et al. [45] computed the velocity field at internal points uniformly located along a series of parallel vertical transects, defined between the free surface and the bottom. Using a fairly coarse vertical spacing, they fitted high-order polynomials to the computed velocities and interpolated within those to obtain results over a denser grid of points. They showed that this procedure was accurate when comparing to velocities actually computed with Eq. (10) at the interpolated points.

This approach, however, cannot be used to accurately calculate internal velocities at arbitrary locations near the crest of an overturning wave. Here, instead, we implement a similar approach, but with a method that analytically approximates velocities over a two-dimensional area near the crest and works for overturning free surfaces. In a complex potential framework — in the vertical plane $z = x + i\,y$ (with $i^2 = -1$) — the flow can be approximated as resulting from the superposition of K discrete singularities (poles) located outside the fluid domain. Given the velocities calculated at time t in the NWT along the free surface near the crest, the locations (z_k) and complex strengths (residues, R_k) of these K singularities can be numerically determined to construct the complex potential, $w(z) = \phi(z) + i\,\psi(z)$ (with ψ the streamfunction),

$$w(z,t) = U_{bg}(t)z + C_0(t) + \sum_{k=1}^{K} \left[R_k \ln(z - z_k) + \bar{R}_k \ln(z - \bar{z}_k + 2ih) \right] \qquad (26)$$

where $U_{bg}(t)$ is a uniform background flow, C_0 is the Bernoulli gauge coefficient, $z_k(t)$ is the complex position of the k-th singularity in the upper half-plane (in air), $R_k(t)$ is its complex residue (representing combined source and vortex strengths), and the overbar denotes the complex conjugate, and the overdot (e.g., $\dot{z}_k$) denotes the time derivative of these discrete parameters.

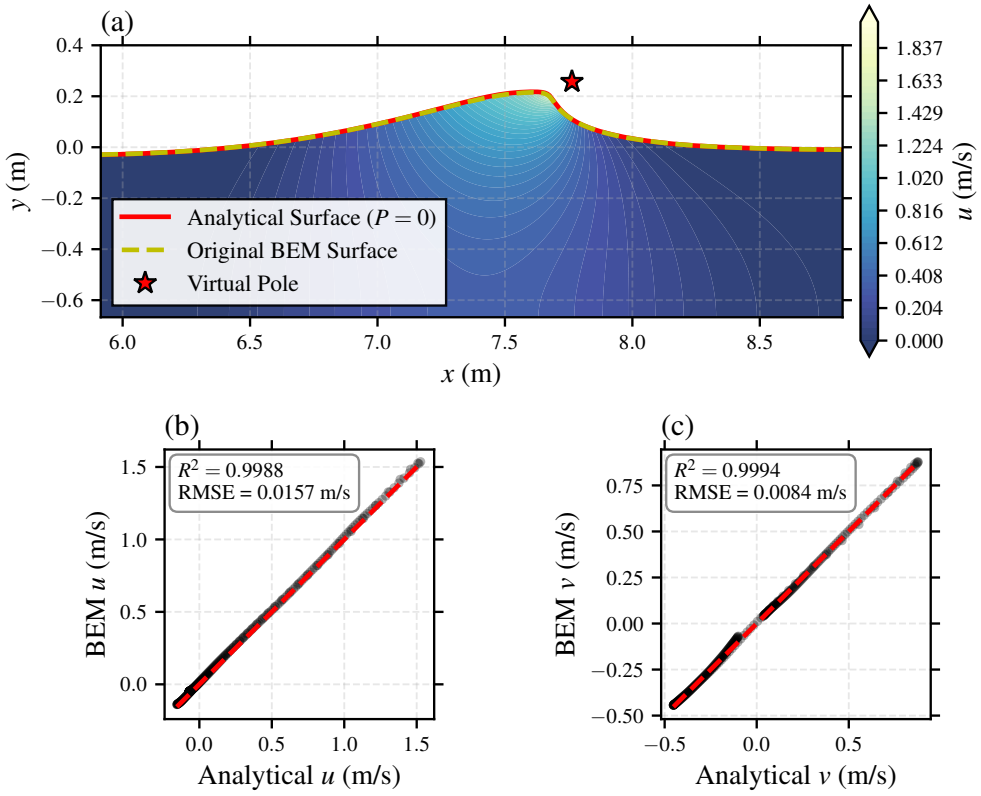


Fig. 9 Test 19. (a) Horizontal velocity field based on NWT results at $t = 126.951\,\mathrm{s}$, approximated by an analytical function with only $K = 3$ poles (Eq. (27); Table 5), as well as the associated free-surface position, both in the NWT and in the approximated solution. (b,c) Least-square fits of free surface velocities computed with the pole model (red) to those in the NWT (black) in the region from $x = 5.91\,\mathrm{m}$ to $8.83\,\mathrm{m}$, which encompasses the locations of WG2 to WG6.

The corresponding complex velocity is then found as the spatial derivative,

$$F(z) = u - iv = \frac{dw}{dz} = U_{bg} + \sum_{k=1}^{K} \left(\frac{R_k}{z - z_k} + \frac{\bar{R}_k}{z - \bar{z}_k + 2ih} \right) \tag{27}$$

where the second term in the sum represents image singularities, enforcing the no-flow condition on the horizontal bottom boundary $y = -h$.

Rather than fitting the potential to the NWT solution directly, we fit Eq. (27) to the computed surface velocities. A very efficient numerical method to do so is the adaptive Antoulas-Anderson algorithm (AAA) [83], which represents analytic functions by a rational approximation. We adopt this approach to robustly provide an initial estimate for the pole locations z_k and residues R_k. These estimates are then refined using a nonlinear least-squares solver to minimize the boundary velocity error and fix

the exact singularity parameters. Once the complex velocity $F(z)$ is calculated, the potential $w(z)$ follows immediately by analytical integration, requiring only a regauging integration (Bernoulli) constant C_0. Given that this analytic function — here both the complex potential and velocity — automatically satisfies Laplace's equation, if the boundary conditions (i.e., on the free surface) are correctly represented, then the internal flow solution is also accurate.

Considering test 19 in the early phases of breaking, say at $t = 126.951\,\mathrm{s}$ when $B = u_c/c_c \approx 0.50$ (Fig. 7), we select a section of the free surface surrounding the crest (from $x = 5.91\,\mathrm{m}$ to $8.83\,\mathrm{m}$). Applying the AAA and least-squares methodology, we find that $K = 3$ poles are sufficient to accurately represent the local kinematics with Eq. (27), yielding Fig. 9. The extracted parameters (z_k, R_k) and U_{bg} are listed in Table 5. We verified that this solution remained accurate when moving away from the crest by comparing both the horizontal and vertical velocity along the free surface. Differences between these were found to be very small and certainly within the experimental uncertainty of the PIV results (Fig. 9b,c).

As an additional assessment of the relevance of the reduced-order method, under the assumption that the flow can be approximated for a short time-duration by the same number of poles, the free-surface corresponding to this approximation of the potential and flow velocity was reconstructed and compared to the free surface computed in the NWT, through using the dynamic free surface boundary condition Eq. (7). This required calculating the time-derivative of the potential, which was obtained by also calculating the time derivatives of the source strengths and locations, i.e., $(\dot{R}_k, \dot{z}_k)$.

To evaluate the dynamic pressure via the unsteady Bernoulli equation, the Eulerian time-derivative of the potential w is required. Thus, taking the partial time-derivative of Eq. (26) yields:

$$w_t(z,t) = \dot{U}_{bg} z + \dot{C}_0 + \sum_{k=1}^{K} \left[\dot{R}_k \ln(z - z_k) - R_k \frac{\dot{z}_k}{z - z_k} + \dot{\bar{R}}_k \ln(z - \bar{z}_k + 2ih) - \bar{R}_k \frac{\dot{\bar{z}}_k}{z - \bar{z}_k + 2ih} \right] \tag{28}$$

(where it is noted that the complex logarithms must be evaluated with branch cuts oriented away from the fluid domain to preserve continuity). The real part of Eq. (28) is the Eulerian time-derivative $\partial\phi/\partial t$ required in Eq. (7), together with the kinetic energy term $\frac{1}{2}|\nabla\phi|^2 = \frac{1}{2} F\,\overline{F}$, to calculate the corresponding free surface elevation.

Returning to test 19 at $t = 126.95$ s, rather than tracking poles over multiple time steps — which introduces finite-difference truncation errors — we exploit Eq. (28). For a given state, the dynamic boundary condition (that the surface pressure is constant) transforms into a linear, overdetermined matrix for the unknown time derivatives $(\dot{R}_k, \dot{z}_k, \dot{U}_{bg}, \dot{C}_0)$. Solving this system on the same BEM collocation nodes, yields the values listed in Table 5. Using these results we compute w_t with Eq. (28), resulting in $\partial\phi/\partial t$, which with the kinetic energy term allows computing the free surface elevation. The latter is compared in Fig. 9 to the NWT free surface elevation, showing an excellent agreement and further confirming the relevance of the method.

Table 6 Complex pole locations (z_k) and strength (R_k) computed with Eq. (27) based on the flow kinematics simulated in the FNPF-BEM-NWT for test 19, at $t = 127.080\,\mathrm{s}$, when $B \simeq 0.85$. For the background flow, $U_b = -0.017\,\mathrm{m/s}$, $\dot{U}_b = 0.564\,\mathrm{m/s^2}$, and the Bernoulli coefficient is $C_0 = -4.125\,\mathrm{m^2/s}$.

	z_k (m)		$\dot{z}_k$ (m/s)		R_k ($\mathrm{m^2/s}$)		$\dot{R}_k$ ($\mathrm{m^2/s^2}$)	
Pole (k)	Re	Im	Re	Im	Re	Im	Re	Im
1	7.976	0.232	1.676	-0.103	-0.061	-0.003	0.095	0.076
2	7.348	0.917	1.004	-1.879	0.623	0.013	-2.393	-0.672
3	8.177	0.575	3.234	-2.340	-0.347	0.011	2.653	0.567

While the instant that $B = 0.50$ may be well-represented by a few poles, for one, the crest had not yet arrived in the field of view of the PIV, and the more demanding check is to consider the moment when $B = 0.85$, which we address next.

4.5 Comparison of computed and measured near-crest velocities

If we advance in time to $B \simeq 0.85$, we see that the same calculation as before results in a singularity approximately the same height as the wave crest itself (Table 6). Despite this fact, the velocities and even the time-derivatives remain sufficiently similar that the free-surface remains well represented (Fig. 10a). There are some slight differences as the NWT solution starts to show an overturning front, but the differences between this analytic approximation and the NWT solution appears to be of a similar order of magnitude as the differences between the numerical solution and the experimental results (Fig. 10b). In order to quantify this velocity variation more precisely, in Fig. 11, we compare velocities along vertical transects at three different locations, corresponding to WG 3, 4, and 5 (from 6.81 m to 8.51 m), and observe a good agreement over the entire range.

To compare the numerical results directly with the PIV experiments, advancing to $B \simeq 1.00$ when the wave crest is fully visible in the video, and knowing that points near the crest may provide erroneous values, we take multiple horizontal transects under the crest and compare the analytic approximation of the NWT results to the PIV measurements Fig. 12); overall, the agreement between both is quite good, with as expected more discrepancies close to the surface. In Fig. 12b,c, along a high transect at $y = 0.12\,\mathrm{m}$, the maximum horizontal velocity occurs under the crest, as expected, and is closely predicted in simulations; in contrast, a large vertical velocity occurs in the front of the wave and small negative vertical velocity on the back side of the wave. Along a lower transect at $y = -0.07\,\mathrm{m}$ (Fig. 12d,e), the agreement of simulations with experiments is still excellent.

While the analytic approximation of the breaking crest is already using fewer degrees of freedom than the BEM solution, it should be possible to further reduce this number. For example, the sum of the $\dot{R}_k$ for both Table 5 and Table 6 is close to zero, which is physically consistent — the near-zero sum of the real and imaginary parts reflects local mass conservation and Kelvin's circulation theorem. In comparison, if

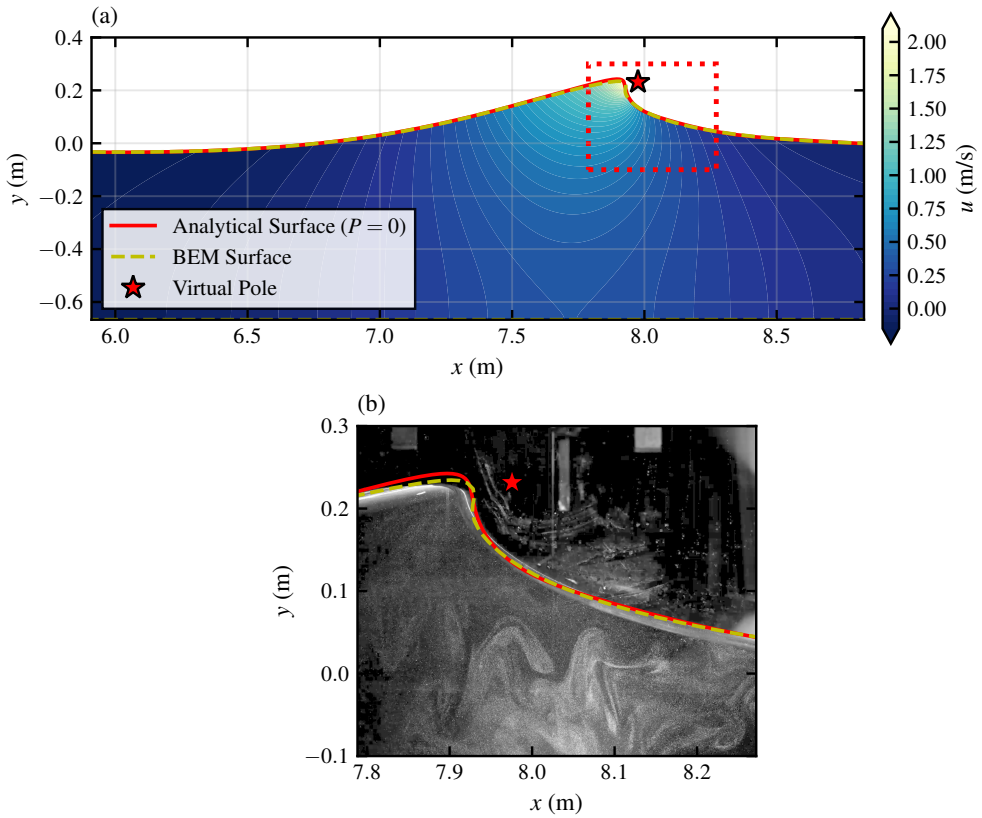


Fig. 10 Test 19. (a) Horizontal velocity field at $t = 127.080\,\mathrm{s}$, when $B \simeq 0.85$, based on NWT results approximated by Eq. (27) with $K = 3$ poles (Table 6), as well as the associated free-surface position, both in the NWT and in the approximated solution. (b) Zoom of (a) on crest, overlaid on the corresponding PIV image. The pole model is fit to the free surface velocities for the region from $x = 5.91\,\mathrm{m}$ to $8.83\,\mathrm{m}$, which are the locations of WG2 to WG6.

we consider Renaud et al. [84], who related for some collection of breaking waves the spatial variation of the kinematics to γ, our results suggest that additional degrees of freedom are likely required to fully specify this. We can further note that, although we did not explicitly consider here the time-evolution of the poles, their movement is predominantly linear, as we would expect for a traveling wave. Given that this representation covers a region of some meters, a natural extension is also to recast the sum of poles as a single multipole expansion, since small variations in the most distant singularity — while necessary for ensuring a consistent fit with the BEM results over several meters of the domain — have little effect on the crest itself.

The basis used in Eq. (27) is similar to the classical asymptotic model of Longuet-Higgins [18], who represented an overturning crest using fractional singularities. While theoretically deep, they are valid only in the immediate vicinity of the crest tip, and add the complexity of handling a branch cut in the velocity field. Alternatively, the

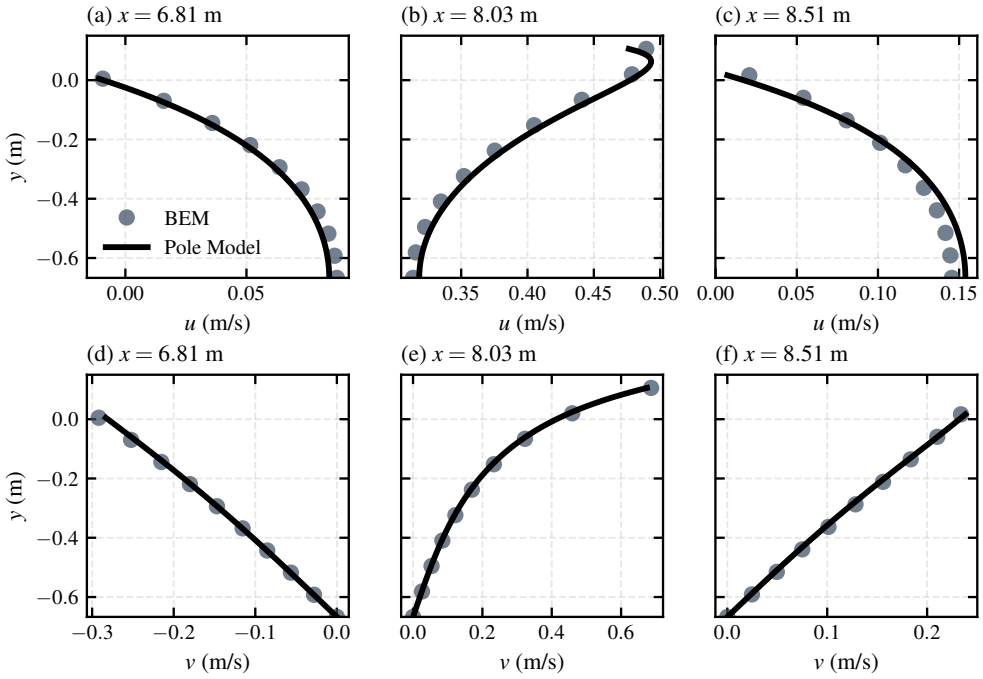


Fig. 11 Test 19. Comparisons of velocity computed using the pole approximation from Eq. (27) (solid lines) with those in the BEM-NWT (bullets), along three vertical transect at $t = 127.080\,\mathrm{s}$, when $B \simeq 0.85$: horizontal velocity (top), and vertical velocity (bottom).

more modern framework by Dyachenko et al. [85] maps the problem to a conformal half-plane or strip. While this offers analytical advantages, our preliminary tests indicate that conformal mapping requires a larger number of parameters to achieve a similar kinematic accuracy to fitting the breaking wave with the $K = 3$ poles considered here. Thus, the reduced rational basis representation of wave-induced velocity fields of Eq. (27), based on simple poles, provides an accurate compression of the BEM solution with a small number of parameters, and this representation captures the localized near-singular behavior. While the basis functions are not globally closed under the exact governing equations, this approach offers a promising framework for reduced-order modeling and for identifying robust indicators of wave breaking. Future work will investigate the time evolution within this basis, identifying further physical constraints to potentially simplify the basis further, and its relation to breaking criteria.

5 Conclusion

In this work, experimentally produced focused plunging breaking waves in the ECM wave flume were measured using wave gauges and a video camera/PIV method, and reconstructed numerically in a fully nonlinear potential flow (FNPF) model, a.k.a.,

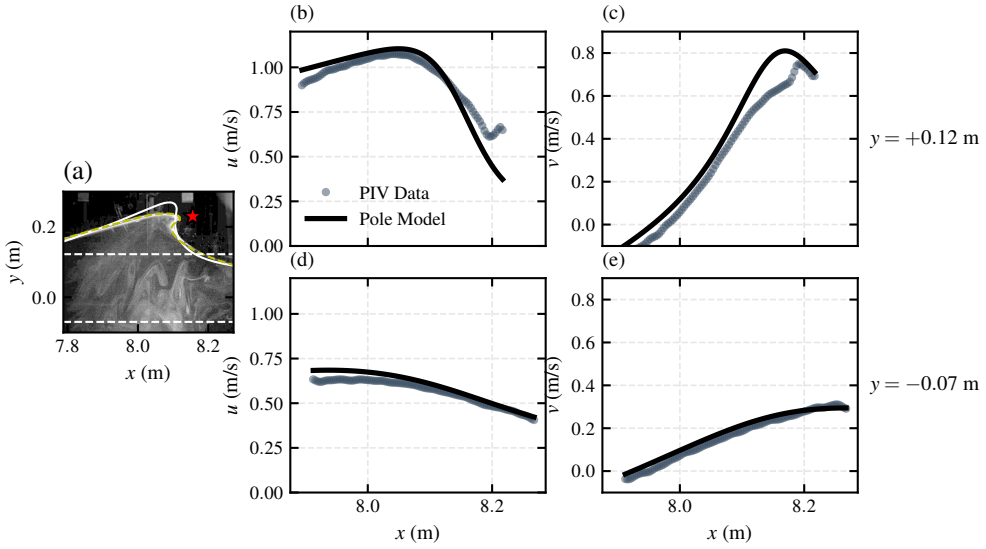


Fig. 12 Comparison of horizontal transect at $t = 127.170\,\mathrm{s}$, when $B \simeq 1.00$ for horizontal velocity (b,d), and vertical velocity (c,e), with PIV measurements (points) and parameterization from Eq. (27) (solid).

numerical wave tank (NWT) based on the Boundary Element Method (BEM). Use of a modified Ricker spectrum for wave generation led to excellent repeatability of results, with the heights of the focused wave between two test runs matching within 0.5 mm. Results of FNPF-BEM-NWT simulations showed good agreement for the free surface evolution, with similar velocity field near the crest at focusing, while not requiring any correction factors to reproduce the waves but only applying the same wavemaker motion to the NWT as the physical wavetank. While the fluid velocity at the exact crest was difficult to measure with PIV, the internal fluid velocities agreed well with model results.

While such NWT-BEM results have been compared to PIV data for many years, this new study has allowed comparison with recent works on the proposed breaking onset criterion of $B = u_c/c_c = 0.85$. The free-surface appears to overturn nearly at the time the value $B = u_c/c_c = 0.85$ is obtained, which may be related to why the criterion appears to be generally applicable. From a modeling point of view, this indicates that this value of B may be attained too late in the breaking process for some FNPF models to use as a breaking onset criterion combined with a wave energy dissipation mechanism [e.g., 13].

After breaking starts, the dissipation rate is estimated to follow roughly the parameterization of Romero et al. [74], which appears to be significantly different than that of Derakhti et al. [5], likely due to the large γ value (or rate of energy dissipation) of this rapidly plunging focused wave, outside of Derakhti et al.'s original dataset. The FNPF-BEM-NWT results, however, appear to be relatively insensitive to the exact value of dissipation rate used at any particular moment.

Our analysis of simplified flow representations near the crest suggests that the wave kinematics can be represented by a small number of singularities located outside of the domain (fitted on NWT results at any given time). Here this representation is a combination of simple poles, unlike the fractional singularities studied by Longuet-Higgins [18], or the poles in a conformal mapped domain studied by Dyachenko et al. [85]. This formulation allows for easy reproduction of the breaking wave state using an analytic approximation, at least up to the overturning point. However, by itself this simplified representation does not allow for a detailed assessment of breaking criteria, which is left out for future work.

Regarding the PIV measurements specifically, although there are difficulties in capturing the precise crest velocities, we observed a good agreement between NWT and PIV data, for the spatial variations in horizontal and vertical velocities a few centimeters below the free-surface.

Due to its accuracy we conclude that the dataset of waves measured in these experiments may be used as an experimental benchmark, both for breaking onset and dissipation. For easier future use by other modelers, this dataset was made available as Supplementary Materials.

Data Availability. The datasets generated and analyzed during the current study will be deposited in a public repository. During the peer-review process, all data supporting the findings of this study are available from the corresponding author upon reasonable request.

Acknowledgements. This work has been carried out at the Energy4Climate Interdisciplinary Center (E4C) of IP Paris, which is in part supported by 3rd Programme d'Investissements d'Avenir [ANR-18-EUR-0006-02], and by the Foundation of Ecole polytechnique (Chaire "Défis Technologiques pour une Énergie Responsable" financed by TotalEnergies). In the US, this work was supported by the National Science Foundation, Physical Oceanography Program, under grant OCE-1947960 to the University of Rhode Island.

Author contributions. J.H. conducted the formal analysis, prepared all figures, and drafted the manuscript text. L.K. designed and conducted the laboratory PIV measurements. S.M. developed the case-specific modifications of the BEM numerical wave tank setup and executed the preliminary simulations. J.M. processed the raw PIV data to extract the spatial and velocity fields. J.D. contributed to the experimental methodology by providing critical guidance on PIV limitations. S.G. contributed extensively to the rewriting, restructuring, and refinement of the text.

A Pictures of laboratory experiments

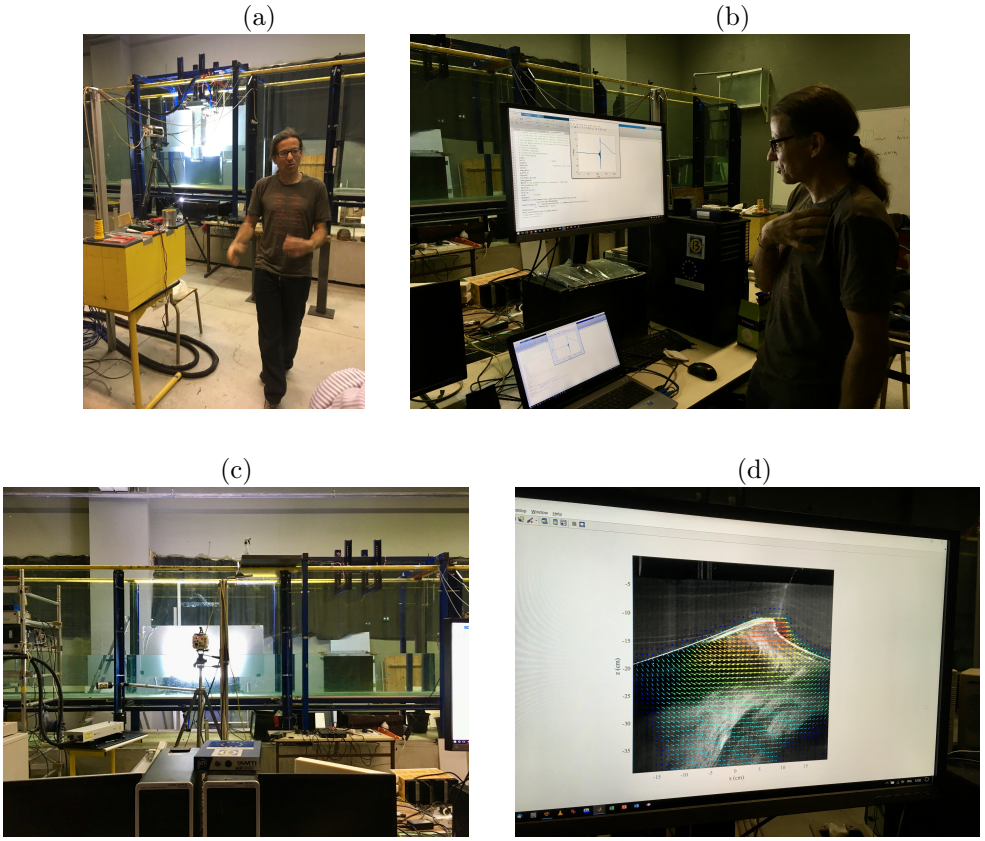


Fig. 13 (a,b) Dr. Kimmoun supervising focused wave breaking experiments in the ECM wave flume; (c) View of experimental set-up with the high-speed camera facing the experimental focusing section; (d) Real time processing of PIV data on the laboratory computer. These experiments are similar to those from 2021 reported in this paper. [Pictures taken by S. Grilli on June 1, 2018]

References

[1] Lee, J., Monty, J., Elsnab, J., Toffoli, A., Babanin, A., Alberello, A.: Estimation of kinetic energy dissipation from breaking waves in the wave crest region. Journal of Physical Oceanography **47**(5), 1145–1150 (2017)

[2] Derakhti, M., Banner, M.L., Kirby, J.T.: Predicting the breaking strength of gravity water waves in deep and intermediate depth. J. Fluid Mech. **848** (2018) https://doi.org/10.1017/jfm.2018.352

[3] Batlle Martin, M., Harris, J.C., Filipot, J.-F., Hulin, F., Tassin, A., Renaud, P.:

Deep water focused breaking wave loads on a fixed cylinder. Coastal Engng. **186**, 104397 (2023)

[4] Derakhti, M., Kirby, J.T., Shi, F., Ma, G.: Wave breaking in the surf zone and deep-water in a non-hydrostatic RANS model. part 1: Organized wave motions. Ocean Modelling **107**, 125–138 (2016) https://doi.org/10.1016/j.ocemod.2016.09.001

[5] Derakhti, M., Kirby, J.T., Banner, M.L., Grilli, S.T., Thomson, J.: A unified breaking onset criterion for surface gravity water waves in arbitrary depth. Journal of Geophysical Research: Oceans **125**(7), 2019–015886 (2020)

[6] Hervouet, J.-M.: Hydrodynamics of Free Surface Flows: Modelling with the Finite Element Method. John Wiley & Sons, England (2007)

[7] Ma, G., Shi, F., Kirby, J.T.: Shock-capturing non-hydrostatic model for fully dispersive surface wave processes. Ocean Modelling **43**, 22–35 (2012)

[8] Ferrand, M., Harris, J.C.: Finite volume arbitrary Lagrangian-Eulerian schemes using dual meshes for ocean wave applications. Computers & Fluids **219**, 104860 (2021)

[9] Shi, F., Kirby, J.T., Harris, J.C., Geiman, J.D., Grilli, S.T.: A high-order adaptive time-stepping TVD solver for Boussinesq modeling of breaking waves and coastal inundation. Ocean Modelling **43**, 36–51 (2012)

[10] Clamond, D., Dutykh, D., Mitsotakis, D.: Conservative modified Serre–Green–Naghdi equations with improved dispersion characteristics. Communications in Nonlinear Science and Numerical Simulation **45**, 245–257 (2017)

[11] Engsig-Karup, A.P., Bingham, H.B., Lindberg, O.: An efficient flexible-order model for 3D nonlinear water waves. Journal of computational physics **228**(6), 2100–2118 (2009)

[12] Harris, J.C., Dombre, E., Benoit, M., Grilli, S.T., Kuznetsov, K.I.: Nonlinear time-domain wave-structure interaction: A parallel fast integral equation approach. International Journal for Numerical Methods in Fluids **94**(2), 188–222 (2022)

[13] Grilli, S.T., Horrillo, J., Guignard, S.: Fully nonlinear potential flow simulations of wave shoaling over slopes: Spilling breaker model and integral wave properties. Water Waves **2**, 263–297 (2020)

[14] Kennedy, A.B., Chen, Q., Kirby, J.T., Dalrymple, R.A.: Boussinesq modeling of wave transformation, breaking, and runup. i: 1d. Journal of waterway, port, coastal, and ocean engineering **126**(1), 39–47 (2000)

[15] John, F.: Two-dimensional potential flows with a free boundary. Communications on Pure and Applied Mathematics **6**(4), 497–503 (1953)

[16] New, A.: A class of elliptical free-surface flows. Journal of Fluid Mechanics **130**, 219–239 (1983)

[17] Greenhow, M.: Free-surface flows related to breaking waves. Journal of Fluid Mechanics **134**, 259–275 (1983)

[18] Longuet-Higgins, M.: Parametric solutions for breaking waves. Journal of Fluid Mechanics **121**, 403–424 (1982)

[19] Bonmarin, P.: Geometric properties of deep-water breaking waves. Journal of fluid mechanics **209**, 405–433 (1989)

[20] Varing, A., Filipot, J.-F., Grilli, S., Duarte, R., Roeber, V., Yates, M.: A new definition of the kinematic breaking onset criterion validated with solitary and quasi-regular waves in shallow water. Coastal Engineering **164**, 103755 (2021)

[21] Barthelemy, X., Banner, M.L., Peirson, W.L., Fedele, F., Allis, M., Dias, F.: On a unified breaking onset threshold for gravity waves in deep and intermediate depth water. J. Fluid Mech. **841**, 463–488 (2018)

[22] Scolan, Y.-M., Etienne, S.: Pressure analysis in nonlinear waves by revisiting the breaking wave onset. European Journal of Mechanics-B/Fluids **101**, 246–256 (2023)

[23] Hasan, S., Sriram, V., Selvam, R.P.: Evaluation of an eddy viscosity type wave breaking model for intermediate water depths. European Journal of Mechanics-B/Fluids **78**, 115–138 (2019)

[24] Mohanlal, S., Harris, J.C., Yates, M.L., Grilli, S.T.: Unified depth-limited wave breaking detection and dissipation in fully nonlinear potential flow models. Coastal Engineering **183**, 104316 (2023)

[25] Grilli, S.T., Skourup, J., Svendsen, I.: An efficient boundary element method for nonlinear water waves. Engng. Analysis with Boundary Elemts. **6**(2), 97–107 (1989)

[26] Grilli, S.T., Subramanya, R.: Numerical modeling of wave breaking induced by fixed or moving boundaries. Computational Mechanics **17**(6), 374–391 (1996) https://doi.org/10.1007/BF00363981

[27] Guignard, S., Grilli, S.T.: Modeling of wave shoaling in a 2D-NWT using a spilling breaker model. In: Proceedings of the 11th International Offshore and Polar Engineering Conference, vol. 3, pp. 116–123 (2001). International Society of Offshore and Polar Engineers

[28] Hulin, F., Prevosto, M., Tassin, A., Filipot, J.-f., Jacques, N., Grilli, S.: Breaking onset and breaking strength of focused wave packets: Linear prediction model and nonlinear numerical simulations. Coastal Engineering **197**, 104660 (2025)

[29] Mohanlal, S., Harris, J.C., Yates, M.L., Grilli, S.T.: Simulation of depth-limited breaking waves in a 3D fully nonlinear potential flow model. Journal of Waterway, Port, Coastal, and Ocean Engineering **150**(4), 04024007 (2024)

[30] Grilli, S.T., Subramanya, R., Svendsen, I.A., Veeramony, J.: Shoaling of solitary waves on plane beaches. J. Waterway, Port, Coastal, and Ocean Engineering **120**(6), 609–628 (1994)

[31] Grilli, S.T., Svendsen, I.A., Subramanya, R.: Breaking criterion and characteristics for solitary waves on slopes. J. waterway, port, coastal, and ocean engineering **123**(3), 102–112 (1997)

[32] Camfield, F.E., Li, Y., Raichlen, F., Grilli, S.T., Svendsen, I.A., Subramanya, R.: Discussions and closure: Breaking criterion and characteristics for solitary waves on slopes. J. Waterway, Port, Coastal, and Ocean Engineering **124**(6), 329–335 (1998)

[33] Guyenne, P., Grilli, S.T.: Numerical study of three-dimensional overturning waves in shallow water. Journal of Fluid Mechanics **547**, 361–388 (2006) https://doi.org/10.1017/S0022112005007535

[34] Fochesato, C., Grilli, S.T., Guyenne, P.: Note on non-orthogonality of local curvilinear co-ordinates in a three-dimensional boundary element method. International Journal for Numerical Methods in Fluids **48**(3), 305–324 (2005) https://doi.org/10.1002/fld.838

[35] Grilli, S.T., Guyenne, P., Dias, F.: A fully nonlinear model for three-dimensional overturning waves over arbitrary bottom. International Journal for Numerical Methods in Fluids **35**(7), 829–867 (2001)

[36] Narayanan, C., McCalpin, J.D.: Vertical structure of horizontal velocity in regular shoaling waves. Journal of Waterway, Port, Coastal, and Ocean Engineering **123**(3), 130–136 (1997)

[37] Dommermuth, D.G., Yue, D.K., Lin, W., Rapp, R., Chan, E., Melville, W.: Deep-water plunging breakers: a comparison between potential theory and experiments. Journal of Fluid Mechanics **189**, 423–442 (1988)

[38] Na, B., Chang, K.-A., Lim, H.-J.: Flow kinematics and air entrainment under laboratory spilling breaking waves. Journal of Fluid Mechanics **882**, 15 (2020)

[39] Longuet-Higgins, M.S., Cokelet, E.: The deformation of steep surface waves on water-i. a numerical method of computation. Proceedings of the Royal Society of

London. A. Mathematical and Physical Sciences **350**(1660), 1–26 (1976)

[40] Griffiths, M., Easson, W., Greated, C.: Measured internal kinematics for shoaling waves with theoretical comparisons. Journal of waterway, port, coastal, and ocean engineering **118**(3), 280–299 (1992)

[41] Chang, K.-A., Liu, P.L.-F.: Measurement of breaking waves using particle image velocimetry. In: Coastal Engineering 1996, pp. 527–536 (1996)

[42] Skyner, D.: A comparison of numerical predictions and experimental measurements of the internal kinematics of a deep-water plunging wave. Journal of Fluid Mechanics **315**, 51–64 (1996)

[43] Dold, J., Peregrine, D.: An efficient boundary-integral method for steep unsteady water waves. Numerical Methods for Fluid Dynamics II, 671–679 (1986)

[44] Qiao, H., Duncan, J.H.: Gentle spilling breakers: crest flow-field evolution. Journal of Fluid Mechanics **439**, 57–85 (2001)

[45] Grilli, S.T., Gilbert, R.W., Lubin, P., Vincent, S., Astruc, D., Legendre, D., Duval, M., Kimmoun, O., Branger, H., Devrard, D., *et al.*: Numerical modeling and experiments for solitary wave shoaling and breaking over a sloping beach. In: ISOPE International Ocean and Polar Engineering Conference, p. (2004). ISOPE

[46] Kimmoun, O., Branger, H., Zucchini, B.: Laboratory PIV measurements of wave breaking on a beach. In: ISOPE International Ocean and Polar Engineering Conference, p. (2004). ISOPE

[47] Scolan, Y.-M., Kimmoun, O., Branger, H., Remy, F.: Nonlinear free surface motions close to a vertical wall. influence of a local varying bathymetry. In: 22th Water Waves and Floatting Bodies Symposium, vol. 1, pp. 1–4 (2007)

[48] Kimmoun, O., Branger, H.: A particle image velocimetry investigation on laboratory surf-zone breaking waves over a sloping beach. Journal of Fluid Mechanics **588**, 353–397 (2007)

[49] Emarat, N., Forehand, D.I., Christensen, E.D., Greated, C.A.: Experimental and numerical investigation of the internal kinematics of a surf-zone plunging breaker. European Journal of Mechanics-B/Fluids **32**, 1–16 (2012)

[50] She, K., Easson, W.: Experimental study of three-dimensional breaking wave kinematics. Applied Ocean Research **19**(5-6), 329–343 (1997)

[51] Xue, Q., Liang, S., Sun, Z., Xu, Y., Tian, Z.: Near-surface characteristics of velocity profile and momentum transport after wave-breaking in deep water. Ocean Engineering **276**, 114223 (2023)

[52] Govender, K., Mukaro, R., Mocke, G.: Laboratory measurements of mean and

turbulence velocities and shear stresses through the wave roller in strong plunging waves. Coastal Engineering **180**, 104254 (2023)

[53] Düz, B., Lindeboom, R., Scharnke, J., Helder, J., Bandringa, H.: Comparison of breaking wave kinematics from numerical simulations with PIV measurements. In: International Conference on Offshore Mechanics and Arctic Engineering, vol. 57748, pp. 07–06053 (2017). American Society of Mechanical Engineers

[54] Düz, B., Scharnke, J., Hallmann, R., Tukker, J., Khurana, S., Blanchard, K.: Comparison of the CFD results to PIV measurements in kinematics of spilling and plunging breakers. In: International Conference on Offshore Mechanics and Arctic Engineering, vol. 84386, pp. 06–06065 (2020). American Society of Mechanical Engineers

[55] Lu, H., Wang, Q., Liu, H.: An investigation of jet in plunging wave using an improved PIV method. In: ISOPE International Ocean and Polar Engineering Conference, p. (2023). ISOPE

[56] Emarat, N., Christensen, E.D., Forehand, D.I., Mayer, S.: A study of plunging breaker mechanics by PIV measurements and a Navier-Stokes solver. In: Coastal Engineering 2000, pp. 891–901 (2000)

[57] Ghosh, S., Reins, G., Koo, B., Wang, Z., Yang, J., Stern, F.: Plunging wave breaking: EFD and CFD. In: International Conference on Violent Flows (2007). National University Fukuoka, Japan

[58] Lande, Ø., Jensen, A., Johannessen, T.B.: A laboratory experiment and procedure for deterministic validation of numerical wave models. Journal of Fluid Mechanics **1037**, 2 (2026)

[59] Techet, A., McDonald, A.: High speed PIV of breaking waves on both sides of the air-water interface. In: 6th International Symposium on Particle Image Velocimetry, pp. 1–14 (2005)

[60] Belden, J., Techet, A.H.: Simultaneous quantitative flow measurement using PIV on both sides of the air–water interface for breaking waves. Experiments in Fluids **50**(1), 149–161 (2011)

[61] Tondu, C., Gade, M., Morales Meabe, J., Buckley, M.P.: Wide-field-of-view PIV measurements above and below microscale breaking waves. Experiments in Fluids **66**(11), 200 (2025)

[62] Boettger, D.G., Banner, M.L., Barthélémy, X., Keating, S.R., Morison, R.P.: On the energetics of breaking inception and onset in surface gravity waves. arXiv preprint arXiv:2008.00633 (2020)

[63] Lubin, P., Kimmoun, O., Véron, F., Glockner, S.: Discussion on instabilities

in breaking waves: vortices, air-entrainment and droplet generation. European Journal of Mechanics-B/Fluids **73**, 144–156 (2019)

[64] Steer, J.N., Kimmoun, O., Dias, F.: Breaking-wave induced pressure and acceleration on a clifftop boulder. Journal of Fluid Mechanics **929**, 1 (2021)

[65] Kimmoun, O., Ratouis, A., Brosset, L.: Sloshing and scaling: experimental study in a wave canal at two different scales. In: The Twentieth International Offshore and Polar Engineering Conference (2010). OnePetro

[66] Sand, S.E., Mansard, E.: Reproduction of higher harmonics in irregular waves. Ocean Engineering **13**(1), 57–83 (1986)

[67] Grilli, S.T., Subramanya, R.: Quasi-singular integrals in the modeling of nonlinear water waves in shallow water. Engineering Analysis with Boundary Elements **13**(2), 181–191 (1994)

[68] Grilli, S., Svendsen, I.: Corner problems and global accuracy in the boundary element solution of nonlinear wave flows. Engineering Analysis with Boundary Elements **7**(4), 178–195 (1990)

[69] Grilli, S.T., Horrillo, J.: Numerical generation and absorption of fully nonlinear periodic waves. Journal of engineering mechanics **123**(10), 1060–1069 (1997)

[70] Papoutsellis, C.E., Yates, M.L., Simon, B., Benoit, M.: Modelling of depth-induced wave breaking in a fully nonlinear free-surface potential flow model. Coastal Engineering **154**, 103579 (2019) https://doi.org/10.1016/j.coastaleng.2019.103579

[71] Svendsen, I.A., Madsen, P.A., Hansen, J.B.: Wave characteristics in the surf zone. In: Proceedings of the 16th International Conference on Coastal Engineering, pp. 521–539 (1978). American Society of Civil Engineers (ASCE)

[72] Stansell, P., MacFarlane, C.: Experimental investigation of wave breaking criteria based on wave phase speeds. Journal of Physical Oceanography **32**(5), 1269–1283 (2002) https://doi.org/10.1175/1520-0485(2002)032<1269:eiowbc>2.0.co;2

[73] Li, Y., Fuhrman, D.R.: On the turbulence modelling of waves breaking on a vertical pile. Journal of Fluid Mechanics **953**, 3 (2022)

[74] Romero, L., Melville, W.K., Kleiss, J.M.: Spectral energy dissipation due to surface wave breaking. Journal of Physical Oceanography **42**(9), 1421–1444 (2012)

[75] Fedele, F., Banner, M.L., Barthelemy, X.: Crest speeds of unsteady surface water waves. Journal of Fluid Mechanics **899**, 5 (2020)

[76] Fedele, F.: Fold catastrophe in breaking waves. Communications in Nonlinear

Science and Numerical Simulation **161**, 110030 (2026) https://doi.org/10.1016/j.cnsns.2026.110030

[77] Hulin, F.: Experimental study of the hydrodynamic loads generated by breaking wave impacts on floating offshore wind turbines. PhD thesis, ENSTA Bretagne-École nationale supérieure de techniques avancées Bretagne (2024)

[78] Mohanlal, S.: Amélioration de la modélisation 2D et 3D de vagues déferlantes en milieu maritime. PhD thesis, École des Ponts ParisTech (2023)

[79] Drazen, D.A., Melville, W.K., Lenain, L.: Inertial scaling of dissipation in unsteady breaking waves. Journal of Fluid Mechanics **611**, 307–332 (2008) https://doi.org/10.1017/S0022112008002826

[80] Rapp, R.J., Melville, W.K.: Laboratory measurements of deep-water breaking waves. Philosophical Transactions of the Royal Society of London. Series A, Mathematical and Physical Sciences **331**(1622), 735–800 (1990)

[81] Tian, Z., Perlin, M., Choi, W.: Energy dissipation in two-dimensional unsteady plunging breakers and an eddy viscosity model. Journal of fluid mechanics **655**, 217–257 (2010)

[82] Wang, C., Gao, Q., Wang, H., Wei, R., Li, T., Wang, J.: Divergence-free smoothing for volumetric PIV data. Experiments in Fluids **57**(1), 15 (2016)

[83] Nakatsukasa, Y., Sète, O., Trefethen, L.N.: The AAA algorithm for rational approximation. SIAM Journal on Scientific Computing **40**(3), 1494–1522 (2018)

[84] Renaud, P., Hulin, F., Prevosto, M., Filipot, J.-F.: Breaking wave-induced slamming loads on vertical cylinders from underlying linear wave properties and parametric models. Ocean Engineering **356**, 125325 (2026)

[85] Dyachenko, A., Dyachenko, S., Lushnikov, P., Zakharov, V.: Dynamics of poles in two-dimensional hydrodynamics with free surface: new constants of motion. Journal of Fluid Mechanics **874**, 891–925 (2019)